Nucleic Acids Research, 2026, **54**, gkag108
https://doi.org/10.1093/nar/gkag108
Genome integrity, repair and replication

Azoospermia phenotype and scRNA-seq reveal hnRNPK as a factor essential for male germ cell development in mice

Huihui Gao[1,2,†], Shiyu Yang[2,†], Ao Ning[3,†], Lisha Yin[2], Yifei Lan[2], Keren Cheng[4], Wenjing Xiong[5], Xinxin Xiong[2], Jin Zhang[2], Jingshou Chen[2], Shenglei Feng[2], Xu Fan[2], Kuan Liu[2], Yiqian Gui[2], Peng Zhang[1], Xiaoli Wang[2], Fengli Wang[2], Xiaoxu Chen[6,*], Qinghua Zhang[1,*], Shuiqiao Yuan[2,5,7,*]

[1]Department of Obstetrics and Gynecology, The Central Hospital of Wuhan, Tongji Medical College, Huazhong University of Science and Technology, Wuhan 430030, China
[2]Institute of Reproductive Health, Tongji Medical College, Huazhong University of Science and Technology, Wuhan 430030, China
[3]College of Animal Science and Technology, Sichuan Agricultural University Sichuan, Chengdu 625014, China
[4]Center for Reproductive Medicine, The Fourth Affiliated Hospital, Zhejiang University School of Medicine, Yiwu 322000, China
[5]Laboratory Animal Center, Huazhong University of Science and Technology, Wuhan 430030, China
[6]College of Animal Science and Technology, Northwest A&F University, Yangling 712100, China
[7]Shenzhen Huazhong University of Science and Technology Research Institute, Shenzhen 518057, China

*To whom correspondence should be addressed. Email: shuiqiaoyuan@hust.edu.cn
†The first three authors should be regarded as Joint First Authors.

Abstract

The process of male germ cell development is a central determinant of spermatogenesis. Nevertheless, the genetic regulatory mechanisms underlying male germ cell development in mammals remain largely unclear. In this study, employing a germ cell-specific *Hnrnpk* knockout mouse model combined with multi-omics analyses, we identified hnRNPK as a key factor necessary for maintaining normal development in differentiating spermatogonia. Phenotypically, adult mice with germ cell-specific hnRNPK deletion exhibited infertility, characterized by a near-complete absence of spermatocytes in the seminiferous tubules. Single-cell RNA sequencing (scRNA-seq) analysis revealed that hnRNPK deletion induced cell-cycle dysregulation in differentiating spermatogonia, triggering apoptotic cell death. As a consequence, the population of differentiating spermatogonia in the testes is markedly diminished, and these cells fail to undergo proper maturation or successfully enter meiosis. Mechanistically, cytoplasmic hnRNPK exerts its regulatory function at the post-transcriptional level, regulating the translation efficiency (TE) of genes involved in meiosis, the cell cycle, and transcriptional regulation. Furthermore, hnRNPK interacts with and colocalizes with DAZL at the 40S ribosome, thereby modulating the initiation of target messenger RNA translation. In the nucleus, hnRNPK interacts with splicing factors and participates in the splicing of target genes related to germ cell differentiation and meiosis. Collectively, these findings emphasize the functional role and mechanistic involvement of hnRNPK in differentiating spermatogonia, providing valuable insights into the post-transcriptional regulatory mechanisms that govern male germ cell development.

Graphical abstract

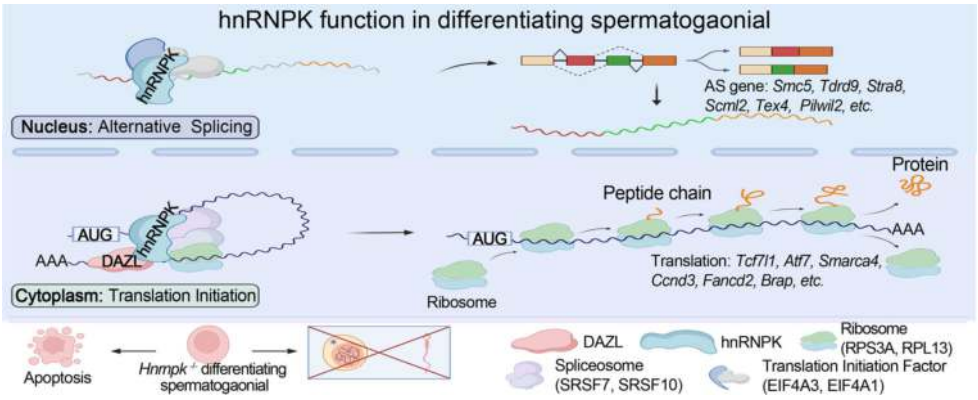

Received: July 24, 2025. **Revised:** January 21, 2026. **Accepted:** January 25, 2026

Introduction

Spermatogenesis is a highly orchestrated developmental program essential for male fertility. Following sex determination in mice, prospermatogonia proliferate until approximately embryonic day E14.5 (E14.5), after which they enter a phase of mitotic quiescence [1]. During the early postnatal period, these cells reinitiate proliferation and migrate toward the periphery of the seminiferous cords. A subset of prospermatogonia differentiate directly into differentiating spermatogonia, initiating the first wave of spermatogenesis. In contrast, another subset gives rise to spermatogonial stem cells (SSCs) around postnatal day 3 (P3), thereby establishing the long-term foundation for subsequent, steady-state spermatogenesis [2–6]. By postnatal day 8 (P8), preleptotene spermatocytes entering meiosis I can be observed, followed by the formation of secondary spermatocytes after completion of the first meiotic division. These cells then undergo meiosis II to produce haploid round spermatids, which then progress through spermiogenesis to produce elongated, functionally mature spermatozoa [7–9]. Perturbations at any step of spermatogenesis can severely compromise sperm output, ultimately leading to non-obstructive azoospermia or oligozoospermia in humans and mice [10, 11]. However, the molecular regulation of these etiologies and pathologies remained incompletely understood.

Heterogeneous nuclear ribonucleoproteins (hnRNPs) constitute a large family of RNA-binding proteins comprising >20 members, which are designated as hnRNP A-U [12]. hnRNP proteins typically harbor modular auxiliary domains enriched in glycine, acidic, or proline residues. Functionally, hnRNPs participate in nearly all aspects of RNA metabolism, including transcription, splicing, 5′ capping, polyadenylation, and translation. They also mediate various nucleic acid processing events, such as telomere maintenance, chromatin remodeling, and DNA repair, which are crucial for physiological and pathological processes [13]. Our previous work demonstrated that members of the hnRNP family are highly expressed in the testes [14]. Several family members regulate distinct stages of germ cell development, including hnRNPG-T [15], hnRNPL [16], hnRNPH1 [17], hnRNPU [18], hnRNPA2B1 [19], hnRNPM [20], and hnRNPC [21]. Deficiency of hnRNPU disrupts the transition from prospermatogonia to spermatogonia, resulting in a Sertoli cell-only phenotype [18]. Two of our previous studies showed that *Stra8*/*Amh*-Cre-mediated depletion of hnRNPH1 leads to meiosis arrest and/or Sertoli cell dysfunction in mice [17, 22]. A recent study in our group revealed that germ cell-specific deletion of hnRNPC causes delayed meiotic entry followed by meiotic arrest [21]. Furthermore, clinical evidence further supports a crucial role between hnRNP protein abnormalities and male infertility. Pathogenic variants in hnRNPG-T have been identified in azoospermic patients [15], and reduced hnRNPL protein levels have been observed in testicular biopsies from men diagnosed with Sertoli cell-only syndrome (SCOS) [16].

As a prominent member of the hnRNP family, hnRNPK was the first protein identified to contain the K-homology (KH) domain, a conserved structural motif that mediates sequence-specific nucleic acid binding [23]. In comparison with other members of the hnRNP family, hnRNPK demonstrates a greater degree of functional versatility and is involved in a broader range of physiological and pathological processes [24]. Global knockout of *Hnrnpk* in mice leads to embryonic lethality [25], underscoring its indispensable role during development. Functionally, hnRNPK acts as a key transcriptional regulator by specifically binding to the promoter regions of proto-oncogenes such as *c-Myc* and *c-Src* and significantly enhancing their transcriptional activity [26–28]. In addition to transcriptional regulation, hnRNPK promotes translation by stimulating internal ribosome entry sites (IRESs)-mediated initiation [29, 30]. Furthermore, hnRNPK modulates alternative splicing (AS) through its interaction with core spliceosomal components [31–33]. Interestingly, the conditional deletion of *Hnrnpk* using *Stra8*-Cre causes spermatocyte arrest at the pachytene stage [34] and impairs the translation of key regulators within the piRNA pathway [35], highlighting the indispensable role of hnRNPK in male fertility. Nevertheless, due to limitations in previous models, the detailed function and molecular mechanism of *Hnrnpk* in regulating spermatogonial remain incompletely understood, despite these findings revealing its biological function in male fertility.

In this study, the *Stra8*-GFP-Cre mouse line was utilized to induce germ cell-specific gene ablation [36], resulting in the deletion of the *Hnrnpk* gene in mouse germ cells. By integrating single-cell RNA sequencing (scRNA-seq) with histological and molecular analyses, we systematically delineated the role of *Hnrnpk* in mouse germ cell development. The loss of *Hnrnpk* impairs the differentiation of spermatogonia and promotes apoptosis, thereby preventing normal developmental progression from entry into meiosis. Mechanistically, hnRNPK functions primarily at the post-transcriptional level, as its deletion significantly reduces the translation efficiency (TE) of genes involved in meiosis, the cell cycle, and transcriptional regulation. Furthermore, we identified hnRNPK as an RNA-binding protein that interacts with DAZL in the cytoplasm to orchestrate translational processes in spermatogonia. Within the nucleus, hnRNPK interacts with splicing factors and participates in the regulation of AS of target genes associated with spermatogonial differentiation and meiosis. Together, these findings define the molecular functions of hnRNPK during the onset of spermatogenesis and highlight a previously unappreciated post-transcriptional regulatory axis governed by hnRNPK in male germ cells.

Materials and methods

Mice and ethics

All mice used in this study were maintained on a genetic background. *Hnrnpk*$^{flox/+}$ mice were obtained from Cyagen Biosciences, in which loxP sites were inserted flanking exons 6–7 of the *Hnrnpk* locus. To generate germ cell–specific conditional knockout mice, we crossed *Hnrnpk*$^{flox/flox}$ mice with *Stra8*-GFPCre mice (kindly provided by Prof. Minhan Tong, Institute of Biochemistry and Cell Biology, CAS) to obtain *Stra8*-GFPCre; *Hnrnpk*$^{flox/+}$ male offspring. These males were then backcrossed with *Hnrnpk*$^{flox/flox}$ females to produce *Stra8*-GFPCre; *Hnrnpk*$^{flox/Del}$ male mice (*Hnrnpk*-cKO). All animals were housed in specific pathogen-free rooms in the Laboratory of Animal Center, Huazhong University of Science and Technology. All animal experiments were conducted ethically and approved by the Institutional Animal Care and Use Committee of Tongji Medical College, Huazhong University of Science and Technology, under animal assurance number S2795. Genotyping was performed by polymerase chain reaction (PCR) using genomic DNA isolated from their tails or toes. The primers used are listed in Supplementary Table S1.

PAS staining

Mouse testes and epididymides were fixed in Bouin's solution (Sigma, Lot #SLBJ3855V) at room temperature (RT) overnight. The tissues were then dehydrated through a graded ethanol series (75%, 80%, 90%, and twice in 100%), cleared in xylene, and subsequently infiltrated and embedded in paraffin. The tissue was sectioned into 5 μm thick slices and incubated with periodic acid (BBI, A600690-0025) and Schiff (Sigma, 1.09033.0500) for 30 min or 10 min, respectively. After dehydration, the slides were mounted with neutral resin (Solarbio, G8590).

Immunofluorescence staining, TUNEL analyses, and EdU labeling

Testes from control and *Hnrnpk*-cKO mice were fixed in 4% paraformaldehyde (Sigma, P6148) and cryoprotected in sucrose gradient (5%, 15%, and 30%). Tissues were then embedded in O.C.T compound (Sakura Finetek, 4583) and sectioned at a thickness of 5 μm. For immunofluorescence (IF) staining, antigen retrieval was conducted using a citrate solution (pH = 6.0), following which the slides were blocked in 5% donkey serum for 1 h at RT. Following an overnight incubation with the primary antibody at 4°C and a subsequent 1 h incubation with the secondary antibody, the slides were mounted using DAPI-containing mounting medium for imaging. Antibodies are provided in Supplementary Table S2. For the TUNEL assay, the slides were treated with PBST and TUNEL solution (Beyotime, C1086). For the EdU proliferation analysis, the mice were injected intraperitoneally with 50 mg/kg of EdU, and the testes were collected 4 h after injection. Testis sections were processed using the BeyoClick™ EdU-488 Cell Proliferation Kit (Beyotime, C0071S) according to the manufacturer's instructions.

Meiotic chromosome spread analyses

Testis tubules were separated and then incubated in hypotonic extraction buffer (HEB buffer, pH 8.2) containing 30 mM Tris, 50 mM sucrose, 17 mM trisodium citrate dihydrate, 5 mM ethylenediaminetetraacetic acid, 0.5 mM DTT, and 1 mM PMSF for a period of 1.5 h at RT. Spermatocytes were released by gentle pipetting in 80 μl of a 100 mM sucrose buffer, with a pH of 8.2. Thereafter, they were spread on slides that had been covered with a fixation buffer (pH 9.2) containing 1% PFA and 0.15% Triton X-100. Following a 2 h incubation in a humidity box at RT, the slides were air-dried and were then washed twice with 0.4% Photo-Flo 200 (Kodak). The slides were stored at −80°C for IF staining. Antibodies used in this assay are listed in Supplementary Table S2.

Isolation of c-KIT positive cells

The testes of control and *Hnrnpk*-cKO mice at P8 were collected and dissociated into a single-cell suspension using a two-step enzymatic digestion protocol, as previously described [37, 38], to preserve cell surface markers. Briefly, tissue fragments were incubated with 1 mg/ml collagenase IV (Thermo Fisher Scientific, catalogue number 17104019) and 5 U/ml DNase I (BioFroxx, catalogue number 1121MG010) for 5 min with gentle agitation. This was followed by four washes with ice-cold DPBS (Procell, catalogue number PB180329) to remove residual enzyme. The samples were then digested with TrypLE Express (Thermo Fisher Scientific, 12604013) for 3–4 min until a single-cell suspension was achieved. After passing through a 40 μm strainer, the cells were then incubated with magnetic microbeads conjugated to c-KIT antibodies (Miltenyi Biotec, 130-091-224), which were specific to the target surface antigen. This process was conducted in accordance with the manufacturer's recommendations. After gentle washing to remove unbound beads, the labeled cells were passed through a pre-equilibrated magnetic column placed in a separation unit. The magnet-retained (positive) and flow-through (negative) fractions were subsequently collected in separate containers. The efficiency and purity of sorting were then assessed by immunofluorescence using lineage-specific markers. All procedures were performed at 4°C or on ice to maintain cell viability and reduce nonspecific binding.

Cell culture, plasmid construction, and transfection

HEK293T, NIH3T3, and GC-1 cells were cultured in DMEM (Procell, PM150210) containing 10% FBS (Albumin Bovine, 4240GR100) and 1% penicillin–streptomycin solution (Biosharp, BL505A). The cells were cultured in a humidified incubator at 37°C with 5% CO_2. All overexpression plasmids were amplified using a PCR strategy with testis coding sequence (CDS) as templates. All overexpression assays were conducted using Lipo8000 transfection reagent (Beyotime, C0533-1.5 ml), and all RNAi assays were performed using INTERFERin® reagent (Polyplus, 101000028). The cells were seeded into 24-well plates, treated with the corresponding reagent, and collected at 64 h after overexpressing the vector transfection or 72 h after interfering with the cells using siRNA.

Immunoprecipitation and western blot

The isolated cells were transferred to an ice-cold western blot/IP lysis buffer (Beyotime, P0013) and centrifuged at 12 000 × *g* for 10 min at 4°C. For immunoprecipitation, Protein A/G Magnetic Beads (MCE, HY-K0202) were pre-incubated with 4 μg of the antibody, followed by the addition of clarified lysates. The mixture was rotated at 4°C overnight. Immune complexes were collected using a magnetic stand, washed, and subsequently subjected to western blot analysis. For the western blot assay, the protein lysates were loaded onto sodium dodecyl sulfate–polyacrylamide gel electrophoresis (SDS–PAGE) gels and then transferred onto a PVDF membrane (Bio-Rad). Following incubation with primary and secondary antibodies, the bands were visualized using ECL solutions (Bio-Rad, Clarity™ Western ECL Substrate) and a ChemiDoc XRS+ system (Bio-Rad). The antibodies used are listed in Supplementary Table S2.

qRT-PCR

Total RNA was extracted from control and *Hnrnpk*-cKO mice using TRIzol reagent (Invitrogen, 15596-025), and reverse transcription was performed using a 1st Strand cDNA Synthesis SuperMix for qPCR (Yeasen, 11141ES60), following the manufacturer's instructions. Quantitative reverse transcription PCR (qRT-PCR) was performed using a SYBR Green Master Mix (Yeasen, 11202ES03) on a Bio-Rad real-time PCR detection system. Relative gene expression levels were calculated using the $2^{-\Delta\Delta Ct}$ method, normalized with *Gapdh* as control. All primers used for qPCR are listed in Supplementary Table S1.

Nuclear and cytoplasmic protein extraction

Nuclear and cytoplasmic protein fractionations were isolated using the Nuclear and Cytoplasmic Protein Extraction Kit (Beyotime, P0027), following the manufacturer's protocol. Briefly, cells were washed with ice-cold PBS and lysed in cytoplasmic extraction buffer A containing 1 mM PMSF. Buffer B was then added, after which the sample was centrifuged at 12 000 × *g* for 5 min to collect the cytoplasmic fraction. The remaining pellet was then resuspended in nuclear extraction buffer containing PMSF, vortexed intermittently for 30 min on ice, and centrifuged again to obtain the nuclear fraction. All steps were performed on ice or at 4°C. The protein extracts were stored at −80°C until further use.

Nascent protein synthesis assay

To assess *de novo* protein synthesis, we performed HPG metabolic labeling using the BeyoClick™ HPG-594 Protein Synthesis Assay Kit (Beyotime, P1209L) in accordance with the manufacturer's instructions. GC-1 cells were seeded into six-well plates and transfected with *Hnrnpk*-targeting and negative control siRNA using INTERFERin® (Polyplus, 101000028). After 48 h, the cells were treated with cycloheximide (CHX, 200 μM) to inhibit translation, which served as a negative control for HPG incorporation. The cells were subsequently washed with PBS and incubated in methionine-free, serum-free medium supplemented with 50 μM HPG at 37°C for 30 min. Following labeling, the cells were fixed with 4% paraformaldehyde, permeabilized, and subjected to click chemistry for Alexa Fluor™ 594 conjugation. Nuclei were counterstained using DAPI. Images were acquired using a fluorescence microscope with identical exposure settings. HPG-derived fluorescence intensity was quantified using ImageJ software from at least five randomly selected microscopic fields per condition and normalized to the control group. All experiments were performed in biological triplicates.

IP-MS

The testicular tissue was homogenized in a cell lysis buffer (Western and IP: Beyotime, P0013; protease inhibitor cocktail: MCE, HY-K0010) and rotated at 4°C for 30 min to ensure complete lysis. The lysate was then clarified by centrifugation at 12 000 × *g* for 15 min and the supernatant was pre-cleared using control protein A/G beads to minimize nonspecific binding. For immunoprecipitation, an anti-hnRNPK antibody was incubated with the lysate overnight at 4°C with gentle rotation. The antibody-protein complexes were then captured using protein A/G magnetic beads (MCE, HY-K0202) and extensively washed to minimize background. To release the bound proteins, the beads were resuspended in SDS–PAGE loading buffer and boiled at 95°C for 10 min. The supernatant containing the denatured protein complexes was collected by brief centrifugation and subjected to SDS–PAGE. Following electrophoresis, the gel was stained with Coomassie Brilliant Blue to visualize protein bands. Specific gel regions were carefully excised and sent to Bioprofile Co., Ltd. (Shanghai, China) for proteomic analysis. Prior to LC-MS/MS analysis, which was carried out on a Thermo Scientific Q-Exactive HF-X mass spectrometer, in-gel digestion and peptide extraction were performed. The raw data were processed using MaxQuant software, version 2.0.1.0, and protein identification was carried out against the UniProt mouse reference database. Protein hits were filtered based on peptide scores and false discovery rate (FDR) threshold.

MS-DIA quantitative proteomics analysis

Approximately 100 000 c-KIT-positive differentiating spermatogonia were collected for each proteomic profiling experiment. For each biological replicate, cells were isolated from five control mice and five *Hnrnpk*-cKO mice. In total, three independent biological replicates were performed. First, a spectral library was established by acquiring high-quality, non-redundant peptide (MS/MS spectra) using data-dependent acquisition (DDA). This library then served as a reference for identifying peptides and proteins. Subsequently, sample data were acquired in data-independent acquisition (DIA) mode. These DIA spectra were then processed and aligned with the spectral library, enabling accurate qualitative and quantitative protein identification. Quantitative data analysis was conducted using the MSstats R package to identify differentially expressed proteins (DEPs) between groups. Functional enrichment of these proteins was performed using Metascape (https://metascape.org) [39], with a focus on biological processes associated with meiosis and cell cycle regulation.

scRNA-seq analysis

For scRNA-seq, the testes of control and *Hnrnpk*-cKO mice were dissociated into a single-cell suspension using a gentle enzymatic digestion protocol designed to preserve cell viability. This suspension was then filtered through a 40 μm cell strainer to remove debris. Approximately 10 000 cells were then loaded onto the 10x Genomics Chromium Controller for single-cell gel bead-in-emulsion (GEM) encapsulation. The cells were partitioned into individual GEMs, where messenger RNA (mRNA) was captured and reverse transcribed into complementary DNA (cDNA) within each droplet, in accordance with the manufacturer's protocol. The resulting cDNA was then amplified and used for library preparation, which included adding unique molecular identifiers (UMIs) to accurately quantify gene expression levels. Libraries were constructed and sequenced using an Illumina platform with a minimum depth of 50 000 reads per cell to ensure robust transcriptomic coverage. The libraries were sent to the Wuhan Biobank Company for sequencing and data processing. The raw sequencing data were processed using the Cell Ranger pipeline, where the sequences were aligned to the reference genome and the levels of gene expression were quantified. Downstream analyses were performed in R using the Seurat package to perform quality control, normalization, and dimensionality reduction. Clustering was then performed to identify distinct cell populations and differential gene expression analysis was conducted to identify marker genes for each cluster.

Cellular trajectories were inferred using the Slingshot (v2.8.0) algorithm based on Uniform Manifold Approximation and Projection (UMAP) embeddings, with unsupervised clustering (CellType) used as input. The "USPG" cluster was designated as the root, representing the earliest undifferentiated state, and a semi-supervised approach was applied. Prior to trajectory reconstruction, genes were filtered to retain only those expressed in at least 10 cells, with a minimum raw count of three, to ensure model robustness. For pseudotime using Monocle2 (v2.32.0), raw count matrices were extracted from the Seurat object to create a CellDataSet. Size factors and gene

dispersions were estimated using estimate Size Factors and estimate Dispersions, respectively, for normalization and variance modeling. Differentially expressed genes (DEGs) were selected to identify ordering genes using Seurat's FindAllMarkers function with a significance threshold of $P < .01$. These genes were then used to define the ordering filter. Dimensionality reduction was performed using the DDRTree algorithm, followed by cell ordering to infer developmental pseudotime trajectories. Pseudotime values for individual cells were extracted for downstream analyses.

RIP-seq and RNA-seq analyses

For RIP-seq, the c-KIT$^+$ cells isolated from 80 WT mice were lysed in a buffer containing RNase and protease inhibitors. The lysates were then incubated with hnRNPK antibody before being precipitated with protein A/G beads. After extensive washing to remove nonspecific interactions, the co-precipitated RNAs were extracted using phenol-chloroform, purified, and subjected to library preparation. The libraries were sent to the SeqHealth Company (Wuhan, China) for sequencing, and high-quality sequencing data were generated using the Illumina platform. Raw RIP-seq reads were filtered using fastp (version 0.23.1) to remove adapter sequences, low-quality reads (Q < 20 for > 8% of bases), reads shorter than 18 bp, and reads containing more than five N bases, yielding high-quality clean data. During library construction, each RNA molecule was labeled with a UID. After quality control, reads with the same UID were clustered, and similar reads within each cluster were aligned to correct sequencing errors, producing reliable consensus sequences for accurate quantification. Clean reads were mapped to the mouse reference genome GRCm39 to assess gene expression. RIP-enriched regions were identified via genome-wide *de novo* peak calling using exomePeak, and peak sequences were scanned with HOMER to discover motifs significantly associated with these regions.

For RNA-seq, total RNA was isolated from the c-KIT$^+$ cells using TRIzol reagent, after which mRNA was enriched using poly(A) selection. cDNA libraries were then generated and sequenced. The sequences were then aligned to the reference genome using HISAT2, after which gene expression levels were quantified using featureCounts. Differential expression analysis was performed using DESeq2. Gene ontology (GO) enrichment and pathway analysis were conducted using the DAVID and KEGG databases. Data visualization was achieved through heatmaps, volcano plots, and gene network diagrams using R-based packages such as ggplot2 and Cytoscape.

Polysome profiling

Testicular cells were collected and washed with cold PBS, followed by lysis in a polysome extraction buffer supplemented with RNase inhibitors and protease inhibitors. The lysate was then subjected to centrifugation at high speed to remove cellular debris, after which the remaining fraction containing ribosome-bound polysomes was loaded onto a 10%–50% sucrose gradient. The gradient was then subjected to ultracentrifugation at 100 000 × *g* for 3 h at 4°C. The gradient was subsequently fractionated, and protein was extracted from each fraction. The protein samples were then subjected to a western blot analysis to ascertain the distribution of proteins across different polysome fractions.

Ribo-seq analysis

Ribosome profiling was conducted on c-KIT-positive germ cells, which were isolated from the testes of control and *Hnrnpk*-cKO mice at P8 (~30 000 cells per sample). The lysis of cells was conducted in a polysome extraction buffer, supplemented with RNase inhibitors to preserve ribosome–mRNA complexes. Lysates were treated with nucleases to digest unprotected RNA, leaving ribosome-protected fragments (RPFs). These RPFs were then purified. Library preparation was performed using the QEZ-seq Kit (Neoribo), in accordance with the manufacturer's protocol. Following the processes of sequencing and quality control, a DESeqDataSet object was constructed using the DESeq2 package (v1.42.0). Genes with low expression (defined as counts <10 in fewer than 3 samples) were filtered out. Genes showing significant differences in translational output were identified based on $|\log_2\text{FoldChange (ribo/RNA)}| \geq 1$, with $P < .01$ and FDR < 0.01. Genes with $\log_2\text{FoldChange} \geq 1$ were considered to have reduced translational efficiency (low TE), whereas those with $\log_2\text{FoldChange} < -1$ were defined as having increased translational efficiency (high TE).

Alternative splicing event analysis

Alternative splicing events (ASEs) were identified using replicate Multivariate Analysis of Transcript Splicing (rMATS) [40, 41], encompassing five major types: skipped exons (SE), alternative 5′ splice sites (A5SS), alternative 3′ splice sites (A3SS), mutually exclusive exons (MXE), and retained introns (RI). Events were considered significant if they met the criteria of an FDR < 0.05 and an inclusion level difference ($|\Delta\psi| > 0.1$ or < -0.1.

Statistical analysis

All quantitative data are presented as mean ± SEM. Significance was tested using the two-tailed unpaired Student's *t*-test (∗$P < .05$, ∗∗ $P < .01$, ∗∗∗ $P < .001$, and ∗∗∗∗ $P < .0001$) with Prism 10.1.2 (GraphPad Software). Image processing was done using Photoshop (Adobe) and ImageJ (NIH).

Results

hnRNPK is highly expressed in male germ cells and is indispensable for spermatogenesis in mice

We first analyzed its expression pattern of *Hnrnpk* in mouse testis. Analysis of published scRNA-seq data [42] revealed that the *Hnrnpk* transcript is highly expressed in spermatogonia and spermatocytes, beginning to decline after the diplotene spermatocytes and decreasing more markedly during round spermatids (Supplementary Fig. S1A). Western blot and RT-qPCR analyses of various tissues and developmental testes further validated the expression of both *Hnrnpk* protein and mRNA, which were highly expressed in the testis, reaching the highest levels at P21 (Supplementary Fig. S1B–E). To further clarify the expression pattern of hnRNPK in male germ cells, we performed IF using γ-H2AX and hnRNPK on testis sections from adult mice. The results revealed that hnRNPK was consistently highly expressed in spermatogonia, spermatocytes, and round spermatids, but its signal was almost undetectable in elongated spermatids (Supplementary Fig. S1F). These expression data indicate that hnRNPK may play a role before the spermiogenesis stage.

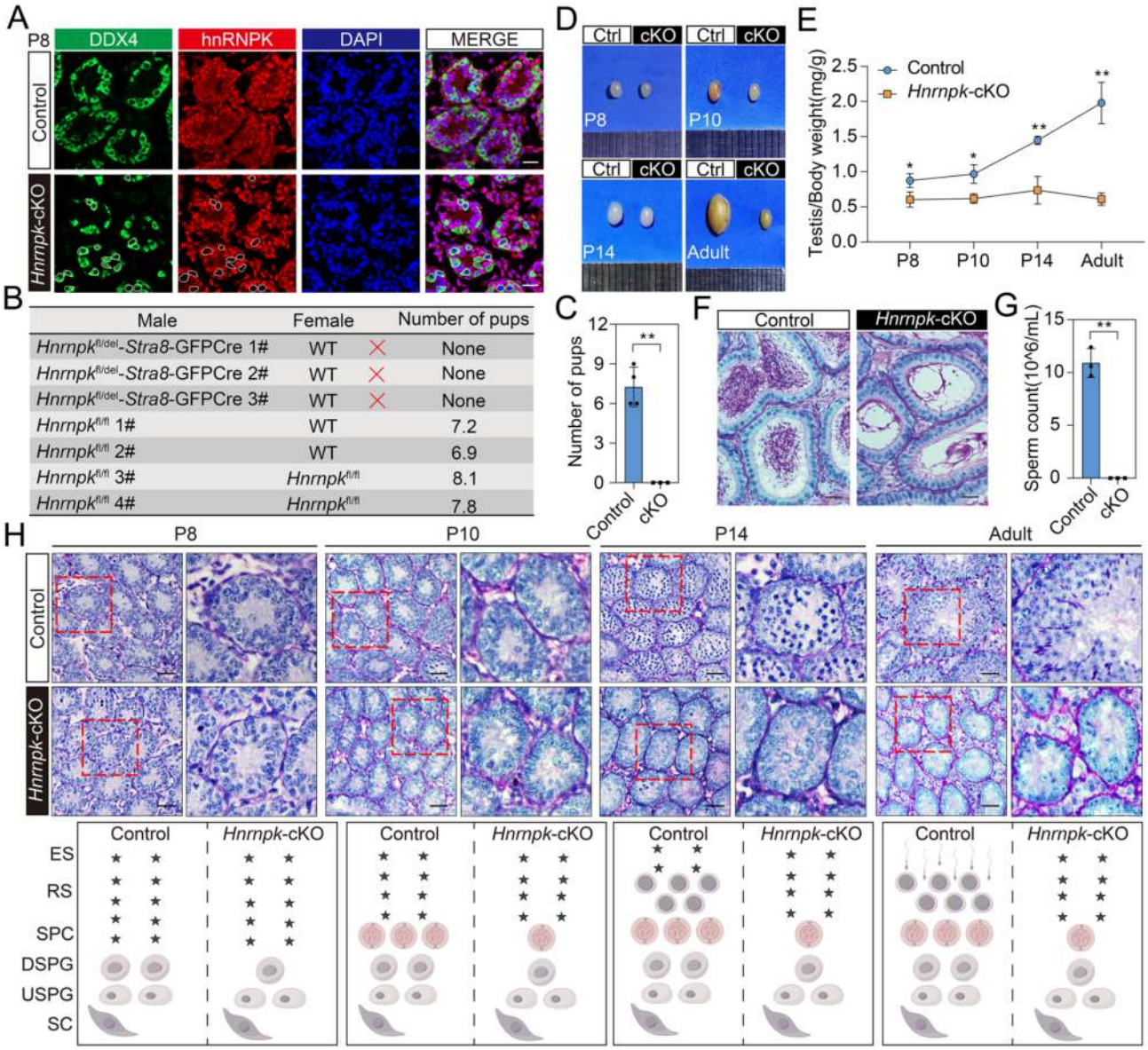

Figure 1. hnRNPK is indispensable for male fertility in mice. (**A**) Validation of hnRNPK knockout efficiency by immunofluorescence staining in testis sections from P8 control and *Hnrnpk*-cKO mice. Sections were stained with anti-hnRNPK (red), anti-DDX4 (green), and DAPI (blue). Scale bars = 20 μm. (**B**) Fertility assay of *Hnrnpk*-cKO males, showing reduced reproductive capability. (**C**) Quantification of litter sizes from adult *Hnrnpk*-cKO male mice (∗∗, $P < .01$). (**D**) Gross morphology of testes from control and *Hnrnpk*-cKO mice at P8, P10, P14, and adult are shown. (**E**) Statistical analysis of the testis-to-body weight ratio in control and *Hnrnpk*-cKO mice at different developmental stages ($n = 3$; ∗, $P < .05$; ∗∗, $P < .01$). (**F**) PAS staining of epididymal cauda sections from adult control and *Hnrnpk*-cKO mice. Scale bars = 50 μm. (**G**) Quantification of sperm counts in epididymal cauda of adult control and *Hnrnpk*-cKO males (∗∗, $P < .01$). (**H**) PAS-stained testis sections from control and *Hnrnpk*-cKO mice at P8 through adulthood, highlighting developmental defects in the seminiferous tubules. The schematic was created using Figdraw. Scale bars = 50 μm.

To further determine the physiological role of hnRNPK in male germ cell development, we created germ cell-conditional *Hnrnpk* knockout mice by utilizing *Stra8*-GFPCre knock-in mouse line [36] to delete the exons 6 and 7 of the *Hnrnpk* gene in germ cells (*Stra8*-GFPCre, *Hnrnpk*$^{lox/Del}$, herein referred to as *Hnrnpk*-cKO or cKO) (Supplementary Fig. S2A–C). The gene recombination is driven by *Stra8*-GFPCre and is initiated at the onset of the type A1 spermatogonial stage [36]. The levels of both mRNA and protein levels of *Hnrnpk* in the adult testes of *Hnrnpk*-cKO mice were significantly lower than in littermate controls (Supplementary Fig. S2D and E), confirming the efficient germline-specific deletion of *Hnrnpk*. Furthermore, IF staining of hnRNPK and DDX4 (a germ cell marker) in P8 and adult testes revealed a marked loss of hnRNPK signal in the germ cells of *Hnrnpk*-cKO mice, while the signal remained normal in somatic cells, confirming the successful deletion of hnRNPK in male germ cells of *Hnrnpk*-cKO mice specifically (Fig. 1A and Supplementary Fig. S3A). Although *Hnrnpk*-cKO males had normal body weights and were viable, they were infertile when subjected to fertility tests (Fig. 1B and C). Moreover, a significant reduction in the testis-to-body weight ratio was observed in *Hnrnpk*-cKO mice starting from P8, in comparison to littermate controls (Fig. 1D and E). Consistent with the reduction in testis size, histological analysis of *Hnrnpk*-cKO males revealed impaired spermatogenesis, evidenced by an absence of mature spermato-

zoa in the cauda epididymis (Fig. 1F and G). Further PAS staining of P8, P10, P14, and adult testes revealed that, starting at P8, the number of germ cells in *Hnrnpk*-cKO testes began to decline, and by P14, a significant loss of spermatocytes was observed within the seminiferous tubules, with only a single layer of cells remaining at the periphery of the tubules in adult *Hnrnpk*-cKO testes (Fig. 1H). In accordance with this observation, it was found that in P6 mice, the number of germ cells (TRA98$^+$ cells) did not show significant changes (Supplementary Fig. S3B); however, in adult mice, there was a severe loss of germ cells (DDX4$^+$ cells), with only sporadic spermatocytes remaining (Supplementary Fig. S3C). The majority of germ cells present within the seminiferous tubules were PLZF-positive undifferentiated spermatogonia (Supplementary Fig. S3D). Together, these results indicate that hnRNPK is required for the development of male germ cells and the maintenance of male fertility in mice.

Ablation of hnRNPK impedes the function of differentiating spermatogonial in mice

As ablation of hnRNPK results in the germ cell loss from P8 onwards, we investigated whether hnRNPK depletion affects the function and differentiation status of differentiating spermatogonia. To this end, we performed IF staining to detect the number of germ cells and differentiating spermatogonia in P6, P8, and adult mice, using DDX4 to mark germ cells and c-KIT to mark differentiating spermatogonia. The results showed that, at P6, there was no significant difference in the number of c-KIT$^+$ cells between *Hnrnpk*-cKO mice and control mice. However, by P8, the number of c-KIT$^+$ cells in the seminiferous tubules of *Hnrnpk*-cKO mice had decreased significantly compared to the control group. In adult *Hnrnpk*-cKO mice, hardly any c-KIT$^+$ cells were observed in the seminiferous tubules (Fig. 2A and B). In addition, we examined the undifferentiated spermatogonia in testes from *Hnrnpk*-cKO and control mice at P8 and in adulthood, using the markers PLZF, SALL4, and CDH1. WT1 staining was performed in parallel to label the Sertoli cells. We found no significant changes in the number of undifferentiated spermatogonia in *Hnrnpk*-cKO mice compared to controls at P8 and adulthood (Supplementary Fig. S4A–F). These results suggest that knocking out *Hnrnpk* resulted in defects in differentiating spermatogonia, leading to a significant decrease in their number.

We then performed co-staining of PLZF, c-KIT, and EdU on the testes of P8 mice to evaluate the proliferation of spermatogonia. The results revealed that the proliferation of undifferentiated spermatogonia (PLZF$^+$EdU$^+$/PLZF$^+$) in the *Hnrnpk*-cKO group did not differ significantly from that of the control group (Supplementary Fig. S4G). However, the c-KIT$^+$EdU$^+$ differentiating spermatogonia was significantly reduced (Supplementary Fig. S5A). Additionally, we found that the number of STRA8$^+$EdU$^+$ cells in P8 *Hnrnpk*-cKO mice and c-KIT$^+$PCNA$^+$ cells in P10 *Hnrnpk*-cKO mice were both markedly lower than in controls, which further confirms the abnormal developmental state of differentiating spermatogonia (Supplementary Fig. S5B and C). Further TUNEL staining revealed that the number of apoptotic cells in *Hnrnpk*-cKO testes was significantly higher than in control groups at P8 and P14 (Fig. 2C and D). Thus, these results suggest that the absence of hnRNPK in germ cells specifically impairs the development of differentiating spermatogonia and triggers apoptosis in germ cells.

Furthermore, we analyzed the SYCP3 and γ-H2AX signals in the testes of P10 and P14 *Hnrnpk*-cKO mice, respectively. The results revealed a significant reduction in the number of SYCP3$^+$ cells in both P10 and P14 mice, demonstrating a marked reduction in spermatocyte numbers upon hnRNPK depletion (Fig. 2E and F). In P14 *Hnrnpk*-cKO mice, the γ-H2AX signal was also significantly reduced, and there was a lack of pachytene and diplotene spermatocytes (Fig. 2G and H). Chromosome spread analysis of P21 testes from control and *Hnrnpk*-cKO mice confirmed that only a few pre-leptotene and leptotene spermatocytes were present in *Hnrnpk*-cKO mice, with no zygotene, pachytene, or diplotene cells observed (Supplementary Fig. S5D and E). Additionally, we observed that the number of STRA8$^+$ cells (differentiating spermatogonia and pre-leptotene spermatocytes) [6, 43] was significantly lower in P10 *Hnrnpk*-cKO mice than in the control group (Fig. 2I and J). We also generated *Ddx4*-Cre^{ERT2}; *Hnrnpk*$^{flox/Del}$ male mice (herein referred to as *Hnrnpk* iKO) for tamoxifen-induced hnRNPK deletion in germ cells by tamoxifen injection at P8 mice for 3 days in order to investigate whether the meiotic process is affected by *Hnrnpk* ablation (Supplementary Fig. S6A). The ablation of hnRNPK in the spermatocytes of *Hnrnpk*-iKO mice was confirmed by IF staining after tamoxifen treatment in P20 mice (Supplementary Fig. S6B). The results of PAS staining and chromosome spread analysis of *Hnrnpk* iKO mice demonstrated a significant reduction in the number of pachytene and diplotene spermatocytes, and an increase in the number of leptotene spermatocytes (Supplementary Fig. S6C–E). These findings suggest that abnormalities occurred during the entry stage of meiosis upon depletion of hnRNPK, resulting in the absence of spermatocytes in the later stages.

scRNA-seq profiling reveals that a deficiency of hnRNPK is associated with spermatogenic failure

To explore the impact of *Hnrnpk* on gene expression at molecular resolution, we performed 10x Genomics scRNA-seq on P10 control and *Hnrnpk*-cKO mice. At this stage, both differentiating spermatogonia and leptotene spermatocytes are present. After filtering the obtained scRNA-seq data for quality, we annotated the cell types and identified four somatic cell types as well as a germ cell population (Supplementary Fig. S7A and B). Various types of cells were evenly distributed between the control and *Hnrnpk*-cKO groups. The dot-plot results showed that each cell population exhibited gene expression patterns consistent with their identity. For instance, germ cells (*Dazl*, *Ddx4*, and *Sycp3*), Sertoli cells (*Amh*, *Sox9*, *Wt1*, and *Gata4*), peritubular myoid cells (*Acta2*, *Tagln*, and *Myl9*), Leydig cells (*Cyp17a1*, *Cyp11a1*, and *Star*), and macrophages and epithelial cells (*Pecam1*, *Cd68*, and *Lyz2*) exhibited high expression within specific cell populations (Supplementary Fig. S7C and Supplementary Table S3). Concurrently, the results of the feature-plot analysis demonstrated that the expression of cell marker genes exhibited marked distinctiveness (Supplementary Fig. S7D), with the top 50 DEGs for each cell group manifesting expression of the corresponding marker genes (Supplementary Fig. S7E). These data confirmed the accuracy of our annotation of testicular cells. Based on this, we counted the proportions of testicular cell subtypes to detect differences between control and *Hnrnpk*-cKO testicular cells. The results demonstrated that, in comparison with the control group, the proportion of germ

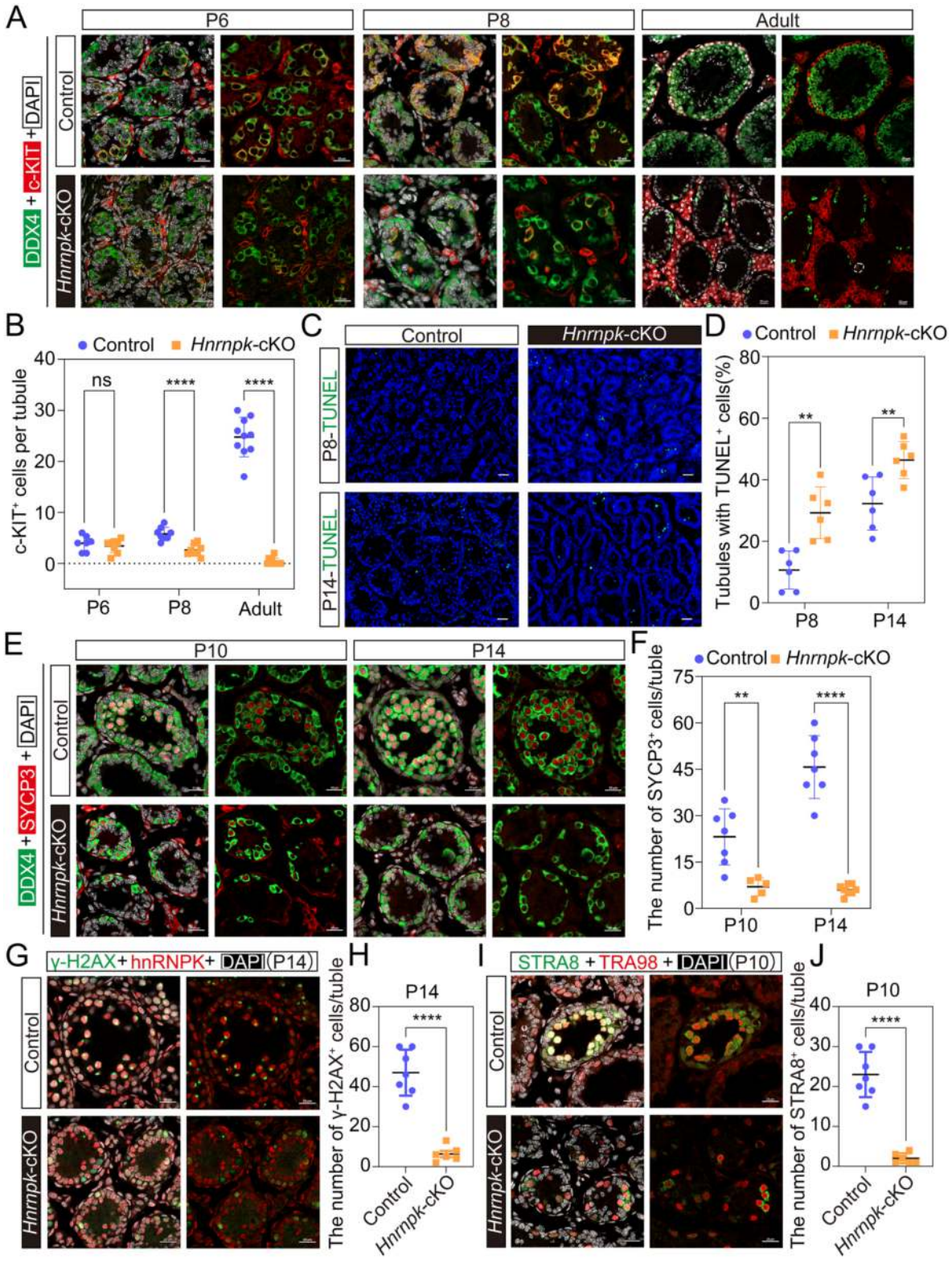

Figure 2. Deletion of hnRNPK leads to the number of differentiating spermatogonial and spermatocyte declines. (**A**) Representative immunofluorescence images of P6, P8, and adult testis sections from control and *Hnrnpk*-cKO mice stained with anti-DDX4 (green), anti-c-KIT (red), and DAPI (white) are shown. Scale bars = 20 μm. (**B**) Quantification of KIT-positive cells per the tubule of P6, P8, and adult mice (ns, no significant; ****, $P < .0001$). (**C**) TUNEL staining showing apoptotic cells in testes from P8 and P14 mice. Scale bars = 50 μm. (**D**) Statistical analysis of the number of tubules with TUNEL-positive cells in each field (**, $P < .01$). (**E**) Immunofluorescence staining of P10, P14 testis sections from control and *Hnrnpk*-cKO mice using anti-SYCP3 (red), anti-DDX4 (green), and DAPI (white). Scale bar = 20 μm. (**F**) Quantification of SYCP3$^+$ cells per tubule for (E). **, $P < .01$, ****, $P < .0001$. (**G**, **H**) Immunofluorescence of P14 testis sections from control and *Hnrnpk*-cKO mice stained with anti-hnRNPK (red), anti-γ-H2AX (green), and DAPI (white) along with quantification of γ-H2AX$^+$ cells (****, $P < .0001$). Scale bars = 20 μm. (**I**, **J**) Immunofluorescence staining of P10 testis sections with anti-TRA98 (red) and anti-STRA8 (green) followed by quantification of STRA8$^+$ cells. Nuclei were counterstained with DAPI (white) (****, $P < .0001$). Scale bars = 20 μm.

cells in the testis of *Hnrnpk*-cKO mice was significantly reduced (Supplementary Fig. S7F), thereby suggesting that germ cells in P10 *Hnrnpk*-cKO mice had already undergone severe developmental abnormalities, a conclusion that is consistent with the results of previous phenotypic experiments.

Further clustering analysis was performed on the identified germ cell population, and the cell types were annotated according to their gene expression patterns (Supplementary Table S4). Four subpopulations of germ cells were identified: undifferentiated spermatogonia (USPG), differentiating spermatogonia (DSPG), leptotene spermatocytes (Lep), and apoptotic germ cells (Fig. 3A and Supplementary Fig. S8A). The USPG cluster exhibited high expression of genes, including *Zbtb16*, *Nanos3*, *Ret*, *Id4*, and *Gfra1*. The DSPG population expressed higher levels of *Kit*, *Stra8*, and *Dmrtb1*. The leptotene cluster showed high expression of meiosis-related genes such as *Mei1*, *Meioc*, *Prdm9*, and *Smc1b*. In addition to these typical germ cell groups, an apoptotic germ cell subpopulation was identified that was characterized by high expression of apoptosis-related genes such as *Cst12*, *Clu* [44, 45], *Gpx8* [46], and *Jun* [47], while also expressing markers associated with differentiating spermatogonia and spermatocytes, such as *Stra8*, *Kit*, and *Meioc* (Supplementary Fig. S8B–D). Quantifying the percentage distribution of these cell types revealed that, compared to the control groups, the proportion of USPG cells increased in the *Hnrnpk*-cKO groups, while the proportion of both leptotene and DSPG cells decreased significantly (Fig. 3B). This decrease in leptotene and DSPG cells was clearly visible in UMAP plots of *Hnrnpk*-cKO mice (Supplementary Fig. S8A). Analysis of DEGs among germ cell subtypes revealed that DSPG cells exhibited a high number of DEGs (Fig. 3C), indicating that hnRNPK deletion primarily impacts the function and development of these cells. GO term analysis of these genes revealed that in DSPG cells, the upregulated genes were implicated in negative regulation of development, apoptosis pathways, and transmembrane transport, while the downregulated genes were associated with DNA recombination, chromatin organization, homologous recombination, and cell cycle process (Fig. 3D). These analyses reveal developmental defects of DSPG, as well as disruptions in cell cycle regulation and increased apoptosis in *Hnrnpk*-cKO mice. This further supports our previous *in vivo* experimental findings that deletion of hnRNPK leads to impaired DSPG cell development.

Furthermore, significant gene expression pattern differences within the DSPG cell population were identified by analysis of the differential gene on the germ cell populations (Supplementary Fig. S9A). A more detailed sub-clustering analysis of the DEGs in DSPG cells was thus performed, resulting in the division of these cells into three subpopulations (DSPG1, DSPG2, and DSPG3) (Supplementary Table S5). Interestingly, we found that DSPG1 showed prominent expression of *Stra8*, *Uchl1*, and *Rbbp4*; DSPG2 exhibited high expression of *Kit*, *Dnmt3b*, and *Dmrt1*; and DSPG3 displayed high expression of *Mov10*, *Cdk8*, and *Cdc42* (Supplementary Fig. S9B). DSPG3 is enriched in genes related to apoptosis and the extracellular matrix, indicating an abnormal, stress-associated differentiating spermatogonial state that accumulates upon hnRNPK deletion (Supplementary Fig. S9C). In addition, the proportions of these three DSPG subpopulations differed between the control and *Hnrnpk*-cKO groups. The proportion of DSPG1 and DSPG2 was found to be lower in the *Hnrnpk*-cKO group in comparison to the control group, while DSPG3 was found to have the highest proportion (67.11% in cKO versus 13.93% in Ctrl) in the *Hnrnpk*-cKO group (Supplementary Fig. S9D). Notably, pseudotime analysis of all germ cells showed that differentiating spermatogonia development was significantly impaired in the *Hnrnpk*-cKO group (Fig. 3E and F). Moreover, a detailed analysis of developmental trajectories using UMAP results revealed two distinct trajectories (Supplementary Fig. S9E). Trajectory 1 primarily followed the developmental path of USPG→DSPG1→DSPG2→leptotene spermatocyte, while trajectory 2 followed USPG→DSPG1→DSPG3→apoptotic germ cells (Fig. 3G). Cell density maps showed that the proportion of leptotene spermatocytes was significantly lower in trajectory 2 than in trajectory 1, while the proportion of DSPG3 and apoptotic cells was markedly higher. Differential expression analysis based on these two distinct developmental trajectories revealed minimal gene expression changes in USPG cells. However, in trajectory 2, there was a significant reduction in the expression levels of genes related to DSPG and meiosis, and a marked increase in the expression levels of genes related to apoptosis (Fig. 3H). Further analysis of the specific gene expression patterns revealed that genes associated with DSPG and the meiotic cell cycle were notably downregulated in the differentiating spermatogonia group in Pseudotime 2. Conversely, apoptotic-related genes were significantly upregulated in the differentiating spermatogonia (Supplementary Fig. S10). The UMAP results showed that cells from the control group were predominantly in trajectory 1, while those from the *Hnrnpk*-cKO group were mainly in trajectory 2 (Fig. 3A and G and Supplementary Fig. S9E). Altogether, these scRNA-seq data indicate that hnRNPK modulates DSPG function, and its absence results in elevated levels of apoptosis, a disrupted cell cycle, and an incapacity to differentiate into spermatocytes within the DSPG population.

Inactivation of hnRNPK results in aberrant transcriptomic profiles in differentiating spermatogonia

To further elucidate the role of hnRNPK in differentiating spermatogonia, we used magnetic-activated cell sorting (MACS) to isolate c-KIT$^+$ spermatogonia from control and *Hnrnpk*-cKO mice at P8. The purity of the isolated cells, as determined by IF staining, consistently exceeded 90% (Supplementary Fig. S11A and B). We then performed transcriptomic (RNA-seq), proteomic, and RIP-seq analyses on the purified cells (Fig. 4A). RNA-seq analysis revealed that 510 genes were upregulated and 513 were downregulated in the *Hnrnpk*-cKO mice. Notably, *Hnrnpk* itself was markedly downregulated (Fig. 4B and Supplementary Table S6). Cell cycle profiling further revealed significant dysregulation, with a notable accumulation of cells arrested in the S phase (Supplementary Fig. S11C and D). GO enrichment analysis showed that the downregulated genes were significantly associated with biological processes such as spermatogenesis, cell cycle progression, and meiotic division (Fig. 4C and D). In contrast, the upregulated genes were predominantly associated with apoptosis, stem cell function, and the MAPK signaling pathway (Fig. 4C and Supplementary Fig. S11E). The expression levels of selected DEGs were further validated by quantitative RT-PCR (Fig. 4E). Therefore, these bioinformatic data suggest that the loss of hnRNPK leads to global

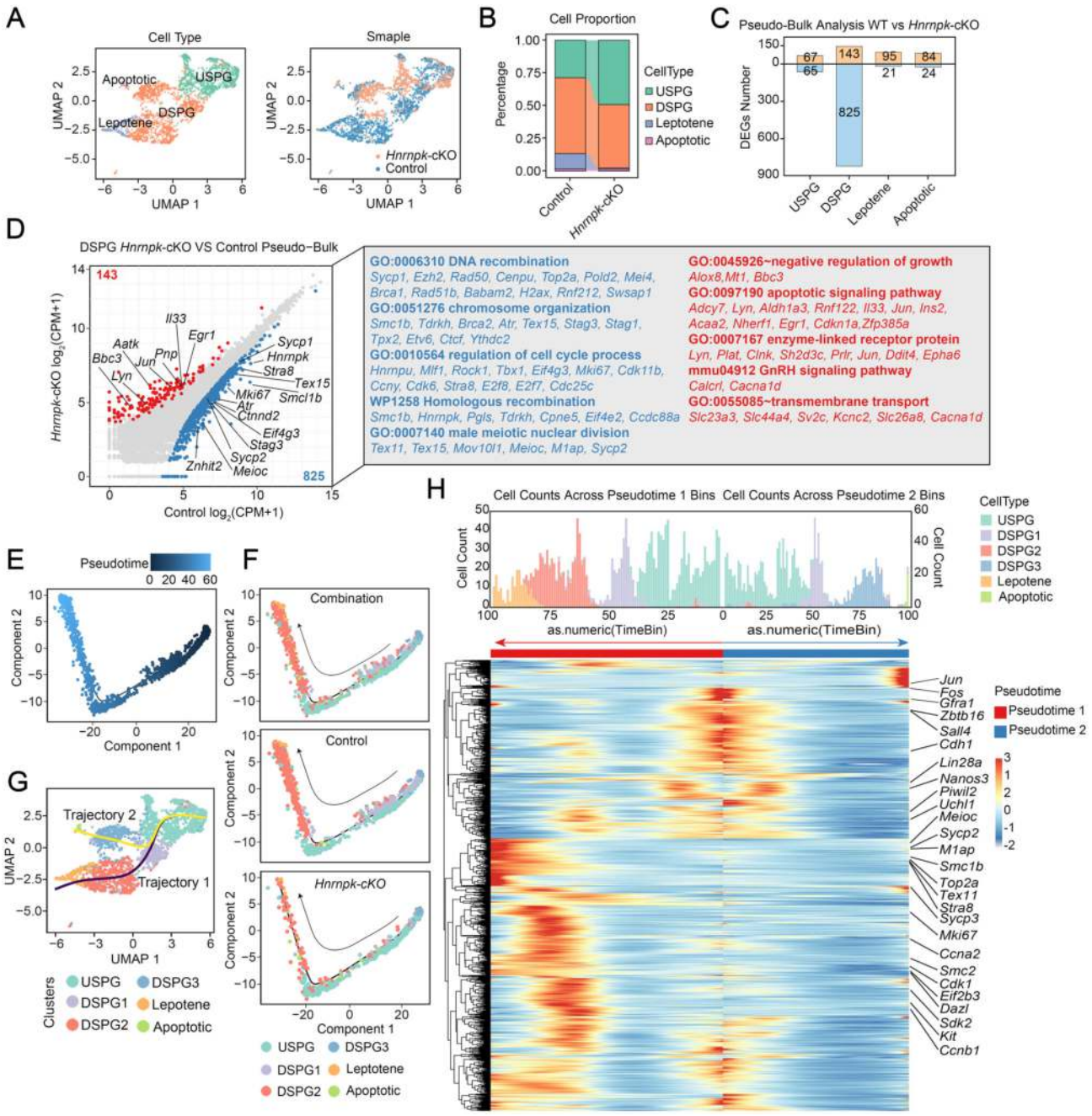

Figure 3. scRNA-seq analysis reveals irregularities in the state of differentiating spermatogonia. (**A**) UMAP visualization of germ cells from P10 testes. The left panel shows integrated clustering of cells from both control and *Hnrnpk*-cKO samples annotated by cell type. The right panel displays UMAP plots of control and *Hnrnpk*-cKO groups separately. (**B**) Bar plot shows the relative proportions of each germ cell type in control and *Hnrnpk*-cKO samples. (**C**) Quantification of DEGs identified in each germ cell subtype between control and *Hnrnpk*-cKO mice. (**D**) Volcano plot illustrates DEGs within the DSPG population. GO enrichment analysis is shown on the right for upregulated and downregulated gene sets, representing distinct biological processes. Genes upregulated in *Hnrnpk*-cKO are highlighted in red; downregulated genes are shown in blue. (**E**) Pseudotime trajectory analysis based on integrated single-cell transcriptomes from control and *Hnrnpk*-cKO testes reveals developmental lineages. (**F**) Pseudotime trajectories from the integrated dataset are shown, with developmental stages annotated by germ cell subtype and separately visualized by sample (control versus *Hnrnpk*-cKO). (**G**) UMAP plot shows inferred developmental trajectories, with purple (Pseudotime trajectories 1) and yellow (Pseudotime trajectories 2) lines indicating two distinct pseudotime paths. (**H**) Cell count distributions across pseudotime bins along two inferred developmental branches. Each bar represents the number of cells per bin, colored by assigned cell types (top). Heatmap shows the expression dynamics of top variable genes ordered along two pseudotime trajectories [red and blue arrows indicate the directionality of the two distinct pseudotime paths, representing potential progression toward meiosis or apoptosis, respectively (bottom)].

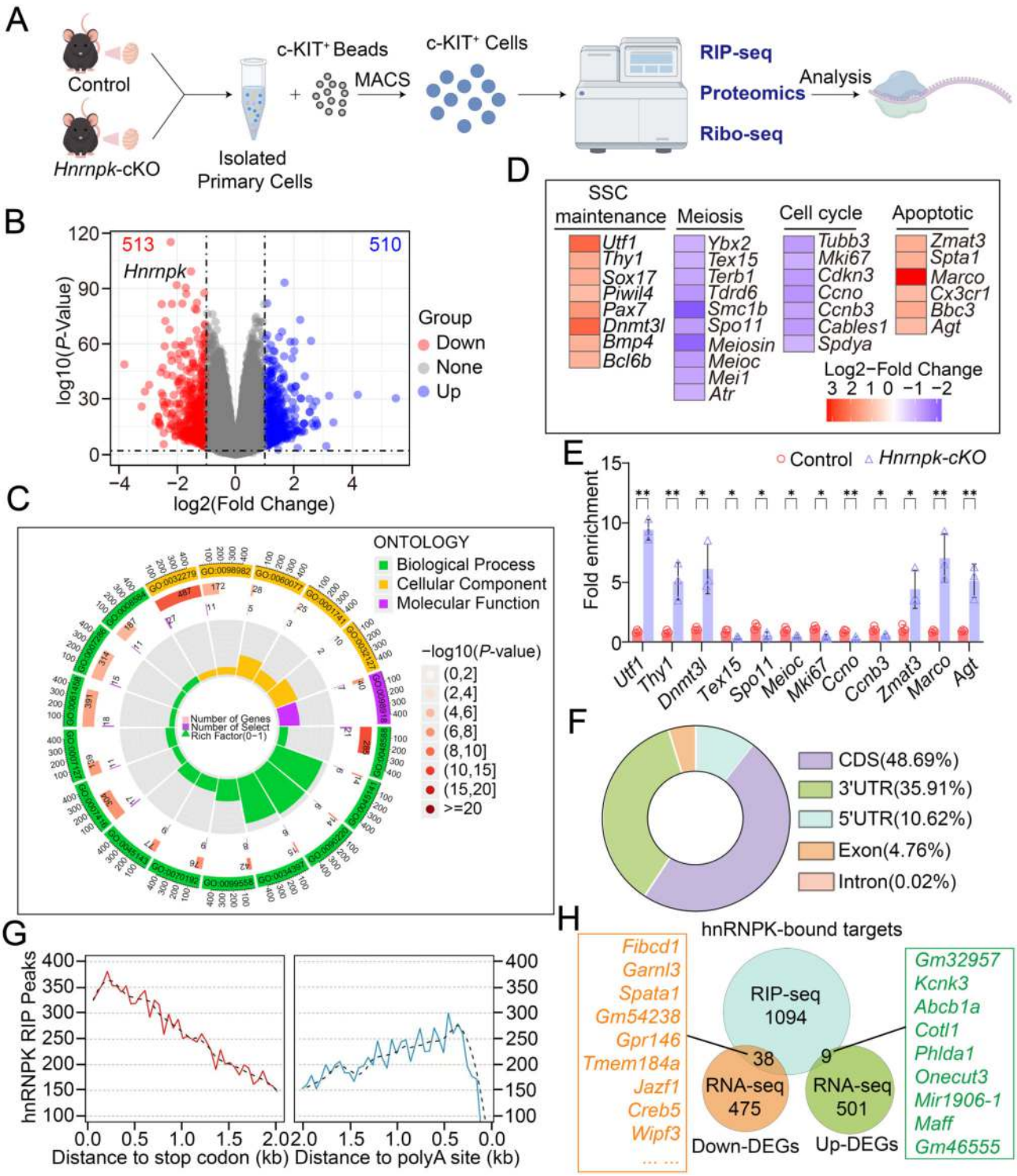

Figure 4. Loss of hnRNPK induces widespread transcriptional dysregulation in differentiating spermatogonia. (**A**) Schematic overview of the downstream experimental workflow for analyzing c-KIT$^+$ germ cells isolated from control and *Hnrnpk*-cKO mice. The schematic was created using Figdraw. (**B**) Volcano plot illustrates DEGs between control and *Hnrnpk*-cKO c-KIT$^+$ germ cells. Genes significantly upregulated in the *Hnrnpk*-cKO are shown in red, downregulated genes in blue, and non-significant genes in gray. (**C**) Circle plot summarizing GO terms enrichment for genes downregulated in *Hnrnpk*-cKO cells. (**D**) Heatmap displays the expression of genes related to SSC maintenance, meiosis, cell cycle, and apoptosis from RNA-seq of c-KIT$^+$ germ cells. Notably, SSC maintenance and apoptosis-related genes were upregulated in the *Hnrnpk*-cKO group, while genes involved in meiosis and cell cycle regulation were significantly downregulated. (**E**) RT-qPCR validation of representative DEGs shown in panel (D), confirming changes in gene expression in control and *Hnrnpk*-cKO c-KIT$^+$ germ cells. (**F**) Pie chart shows the distribution of hnRNPK RIP-enriched regions identified by RIP-seq in c-KIT$^+$ germ cells, categorized by transcript region. (**G**) Metagene analysis of hnRNPK RIP-enriched peaks aligned to the stop codon (left, red line) and polyA site (right, blue line), showing enrichment density in 20 nt bins. (**H**) Venn diagram shows the overlap between hnRNPK-bound transcripts identified by RIP-seq and DEGs from RNA-seq of c-KIT$^+$ germ cells.

transcriptomic perturbation and functional impairment in c-KIT$^+$ differentiating spermatogonia.

Given that hnRNPK is a canonical RNA-binding protein, primarily exerting its function through the regulation of RNA metabolism, we conducted RIP-seq to characterize its RNA interaction profile. RIP-seq analysis revealed that hnRNPK enrichment was predominantly enriched across the CDS, 3′ untranslated region (3′ UTR), and 5′ UTR of target genes (Fig. 4F and Supplementary Fig. S11F), with enrichment of the GCACG motif, as indicated by motif enrichment analysis (Supplementary Fig. S11G). Metagene analysis revealed a pronounced enrichment of RIP-seq signals proximal to the stop codon, with a gradual decline toward the distal 3′ UTR (Fig. 4G). These distributions suggest a preferential association of hnRNPK with the CDS-3′ UTR junction. Overall, hnRNPK was found to target 1141 genes (Supplementary Table S7), many of which are associated with TGF-β signaling, transcription, and Polycomb repressive complex assembly (Supplementary Fig. S11H). Interestingly, of these hnRNPK target genes, 1094 did not exhibit changes in corresponding RNA expression, while only 47 showed both hnRNPK RIP target and altered RNA expression (Fig. 4H), indicating that although hnRNPK modulates spermatogenesis via RNA interactions, its regulatory effects are predominantly post-transcriptional rather than transcriptional.

hnRNPK in the cytoplasm to orchestrate translational processes in spermatogonia

To elucidate the molecular targets of hnRNPK on mRNA translation in germ cells, we conducted a low-input Ribo-seq analysis using c-KIT$^+$ spermatogonia. All libraries exhibited the characteristic 28–30 nucleotide footprint peak, with high read enrichment over CDS (Supplementary Fig. S12A). Furthermore, the presence of strong 3-nucleotide periodicity across biological replicates confirmed the high quality and frame-preserving nature of the ribosome profiling data (Supplementary Fig. S12B and C). By integrating Ribo-seq and RNA-seq datasets (Supplementary Fig. S5A and B), we quantified TE across the control and *Hnrnpk*-cKO groups. A total of 923 transcripts exhibited decreased TE, whereas 964 transcripts showed increased TE upon hnRNPK deletion (Fig. 5B and Supplementary Table S8). GO term analysis revealed that genes with reduced TE were significantly enriched in pathways related to spermatogenesis, meiotic progression, and, interestingly, spliceosome complex assembly, suggesting possible co-translational splicing perturbations in hnRNPK-deficient germ cells (Fig. 5C). Metagene analysis revealed that hnRNPK depletion does not disrupt the overall 3-nt periodicity of ribosome movement along CDS regions. However, a statistically significant reduction in P-site occupancy immediately downstream of the translation start codon, indicating impaired early elongation following translation initiation (Fig. 5D). Of note, a comparison of transcript and ribosome occupancy levels showed that most translational changes occurred independently of mRNA abundance (Supplementary Fig. S12D). This finding further reinforces the notion that hnRNPK acts primarily through post-transcriptional mechanisms. Integration of RIP-seq data with TE alterations revealed that 85 TE-downregulated and 80 TE-upregulated transcripts were hnRNPK-bound targets (Fig. 5E). GO enrichment analysis indicated that TE-downregulated targets were associated with spermatogenesis and RNA polymerase II-related functions (Supplementary Fig. S12E). Targeted validation in c-KIT$^+$ spermatogonia confirmed that key spermatogenesis-related genes—including BRD4 [48], c-KIT [49], SMARCA4 [50], ATF7 [51, 52], and TCF7L1 [52]—exhibited unchanged RNA levels but marked reductions in protein expression (Fig. 5F and G), highlighting impaired translational output following hnRNPK loss.

To further elucidate the underlying mechanism by which hnRNPK regulates germ cell development, we performed an interaction proteomics screen using the testes of P10 mice. A total of 662 candidate proteins that interact with hnRNPK were identified (Fig. 6A and Supplementary Table S9). Functional annotation revealed that these proteins are primarily involved in RNA metabolism, translational regulation, ribosome biogenesis, and splicing (Fig. 6B), suggesting that hnRNPK may coordinate post-transcriptional gene regulation through interaction with these interaction proteins. Subsequent IP experiments corroborated the finding that hnRNPK interacts with spermatogenesis-related regulators DAZL, PIWIL2, and YTHDC2, as well as splicing factors SRSF10 and SRSF7, in an RNA-independent manner (Supplementary Fig. S13A and B). Furthermore, our immunoprecipitation-mass spectrometry (IP-MS) data revealed that hnRNPK interacts with 50 ribosomal proteins (Fig. 6C), as well as with translation initiation regulators such as EIF4A1, EIF4A3, RPS3A, and RPL13 (Figs. 6D and E and Supplementary Fig. S13C). This suggests that hnRNPK plays a role in modulating the translation initiation of target genes. Polysome profiling revealed that hnRNPK predominantly localizes to the RNP fraction and the 40S ribosomal subunit, which provides further evidence for its involvement in controlling translation initiation (Fig. 6F). Knocking down hnRNPK function in GC-1 spermatogonia cell lines resulted in a significant decrease in nascent protein synthesis, as demonstrated by metabolic labeling (Fig. 6G). These results imply that hnRNPK is a crucial regulator of post-transcriptional gene expression, particularly with regard to translation initiation during germ cell development.

We next performed an MS-DIA quantitative proteomic analysis using c-KIT$^+$ spermatogonia that had been isolated. This revealed 902 differentially expressed proteins, of which 483 were found to be upregulated and 419 downregulated (Fig. 6H and Supplementary Table S10). Further GO enrichment analysis showed that the downregulated proteins were significantly enriched in pathways associated with meiotic progression and cell cycle regulation (Fig. 6I). Additionally, correlation analysis of the transcriptomic and proteomic profiles showed poor concordance, suggesting that the observed changes at the protein level are largely independent of transcript abundance (Fig. 6J). This supports the idea that hnRNPK plays a post-transcriptional regulatory role in germ cells.

hnRNPK interacts with DAZL in differentiating spermatogonia

In consideration of the established role of DAZL in regulating TE by enhancing translation of its target mRNAs in male germ cells [53–55], this observation serves to reinforce the hypothesis that hnRNPK is involved in the translation process with DAZL. We then examined the subcellular localization and structural interaction of the hnRNPK-DAZL complex. Both nuclear–cytoplasmic fractionation and IF analyses

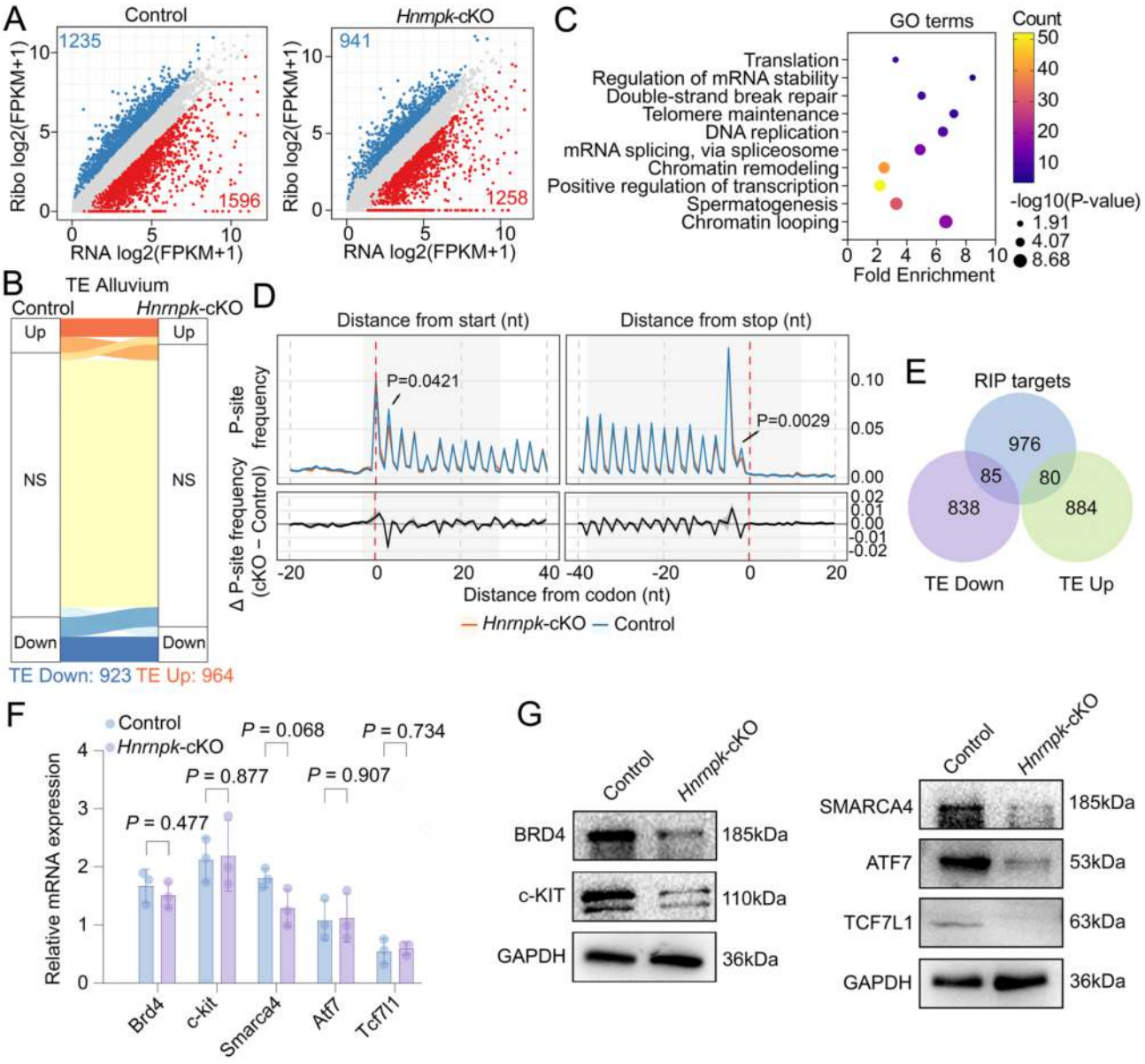

Figure 5. hnRNPK deficiency disrupts TE in c-KIT$^+$ male germ cells. (**A**) Scatter plot comparing RNA abundance (*x*-axis) and ribosome-protected fragment (RPF) abundance (*y*-axis) in c-KIT$^+$ germ cells, based on RNA-seq and Ribo-seq data. Genes with significantly higher TE are highlighted in blue, while those with reduced TE are shown in red. Gray dots represent genes with no significant TE change. Values are shown in $\log_2$(FPKM + 1). (**B**) Alluvial plot illustrates the relationship of TE in control and *Hnrnpk*-cKO c-KIT$^+$ germ cells. Genes are categorized into three classes based on their TE: upregulated (Up), downregulated (Down), and not significantly changed (NS). Genes with differential TE in *Hnrnpk*-cKO c-KIT$^+$ cells compared to controls (bottom). (**C**) GO enrichment analysis of genes with significantly reduced TE in the *Hnrnpk*-cKO group. (**D**) Overlayed metagene profiles of ribosome occupancy across transcripts enriched in *Hnrnpk*-cKO (orange) and control (blue) samples. Upper panels show metagene-averaged P-site frequency across CDS aligned to the translation start (left) or stop (right) codon for control and *Hnrnpk*-cKO samples. Periodic peaks reflect the characteristic 3-nt ribosomal translocation during elongation. Red dashed lines mark the annotated start or stop codon positions. Numerical annotations indicate *P*-values for statistical comparisons proximal to translation start or stop codons. Lower panels display the point-wise difference in mean P-site frequency between *Hnrnpk*-cKO and control samples (Δ P-site frequency = *Hnrnpk*-cKO − control). Shaded regions denote propagated standard errors. (**E**) Venn diagram shows the overlap between hnRNPK-bound transcripts (identified by RIP-seq) and genes with altered TE in the *Hnrnpk*-cKO group. (**F**) RT-qPCR analysis of selected hnRNPK-interacting genes related to spermatogenesis, whose TE was reduced in the *Hnrnpk*-cKO group. mRNA levels were measured in c-KIT$^+$ germ cells. (**G**) Western blot analysis of protein expression for spermatogenesis-related hnRNPK targets with reduced TE in c-KIT$^+$ cells. GAPDH was used as loading control.

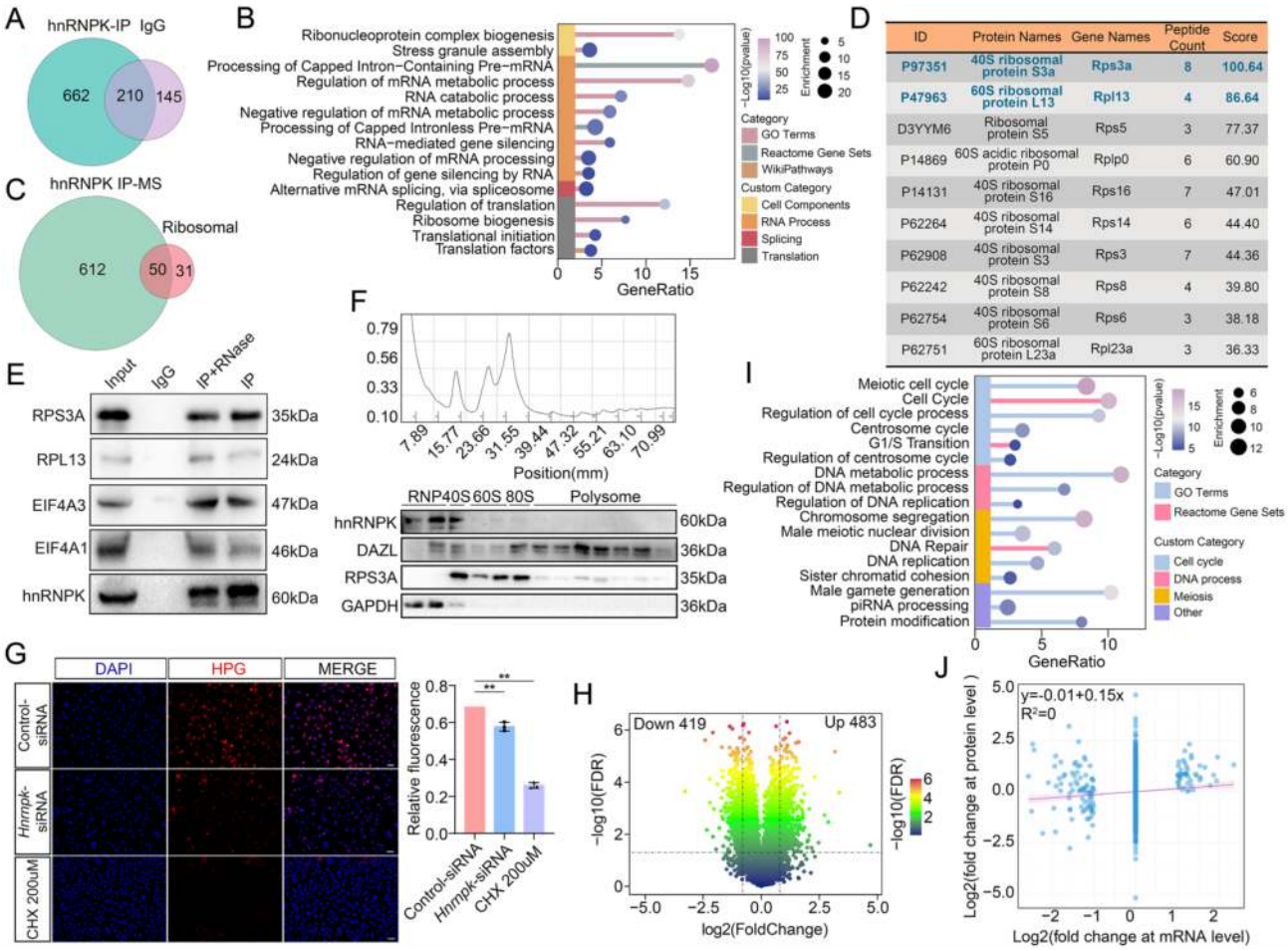

Figure 6. hnRNPK modulates the initiation of protein translation in male germ cells. (**A**) Venn diagram showing the overlap between proteins identified by hnRNPK IP-MS and those detected in the IgG control group from P10 testis lysates. (**B**) Functional annotation of hnRNPK-interacting proteins based on IP-MS results. (**C**) Venn diagram illustrates the overlap between hnRNPK-interacting proteins and annotated ribosomal proteins. (**D**) Table lists the top 10 ribosomal proteins interacting with hnRNPK, ranked by IP-MS enrichment score. (**E**) Co-immunoprecipitation followed by western blot validation of hnRNPK interactions with ribosomal proteins and translation initiation factors in c-KIT$^+$ germ cells. (**F**) Ribosome profiling fractions were collected and subjected to western blotting to assess the distribution of hnRNPK and DAZL across ribosomal subunits and associated complexes. (**G**) Nascent protein synthesis in GC-1 cells measured by HPG incorporation assay under control, *Hnrnpk*-siRNA, and cycloheximide (CHX)-treated conditions. Quantification of relative fluorescence intensity is shown on the right. Scale bars = 20 μm. (**H**) Volcano plot displays differentially expressed proteins between control and *Hnrnpk*-cKO c-KIT$^+$ germ cells. (**I**) Functional annotation of downregulated proteins in *Hnrnpk*-cKO c-KIT$^+$ cells. (**J**) Correlation analysis between mRNA and protein expression levels using the proteomic and transcriptomic data in *Hnrnpk*-cKO c-KIT$^+$ cells.

demonstrated the presence of hnRNPK and DAZL in the cytoplasm of differentiating spermatogonia (Supplementary Fig. S13D and E). Further BiFC assays conducted in NIH3T3, HEK293T, and GC-1 cells also revealed prominent co-localization of hnRNPK and DAZL in the cytoplasm (Supplementary Fig. S13F). To determine the structural basis of this interaction, we generated truncated constructs of MYC-tagged DAZL and HA-tagged hnRNPK, and performed co-immunoprecipitation (co-IP) experiments. These assays demonstrated that the KH1, KH2, and KH3 domains of hnRNPK, along with the DAZ domain of DAZL, are responsible for the physical interaction between the two proteins (Fig. 7A). Interestingly, DAZL protein levels were markedly reduced in hnRNPK-deficient spermatogonia (Fig. 7B), suggesting that loss of hnRNPK destabilizes the hnRNPK-DAZL complex. Cross-referencing known DAZL-bound transcripts [53] with Ribo-seq-derived TE changes further revealed that 124 DAZL targets were translationally downregulated and 102 were upregulated in the *Hnrnpk*-cKO group (Fig. 7C). We conducted further analysis of the changes in the TE of target genes co-regulated by hnRNPK and DAZL, revealing a significant reduction in the efficiency of 18 shared target genes (Fig. 7D). Consistently, protein expression levels of the spermatogenesis-related factors BRAP [56], CCND3 [57], and FANCD2 [58] were markedly lower in the *Hnrnpk*-cKO group (Fig. 7E). These findings suggest that the collapse of the hnRNPK–DAZL regulatory axis upon hnRNPK depletion perturbs DAZL-mediated translation control, thereby contributing to the widespread dysregulation of spermatogenic gene translation.

hnRNPK regulates AS programs critical for male germ cell transcriptome integrity

Ribo-seq analysis revealed that several AS-associated proteins exhibited significantly reduced TE in hnRNPK-deficient germ cells (Fig. 5C) and that hnRNPK physically interacts with multiple AS machinery components (Fig. 6B). Based on these findings, we hypothesized that hnRNPK may serve as a potential regulator of splicing dynamics during male germ

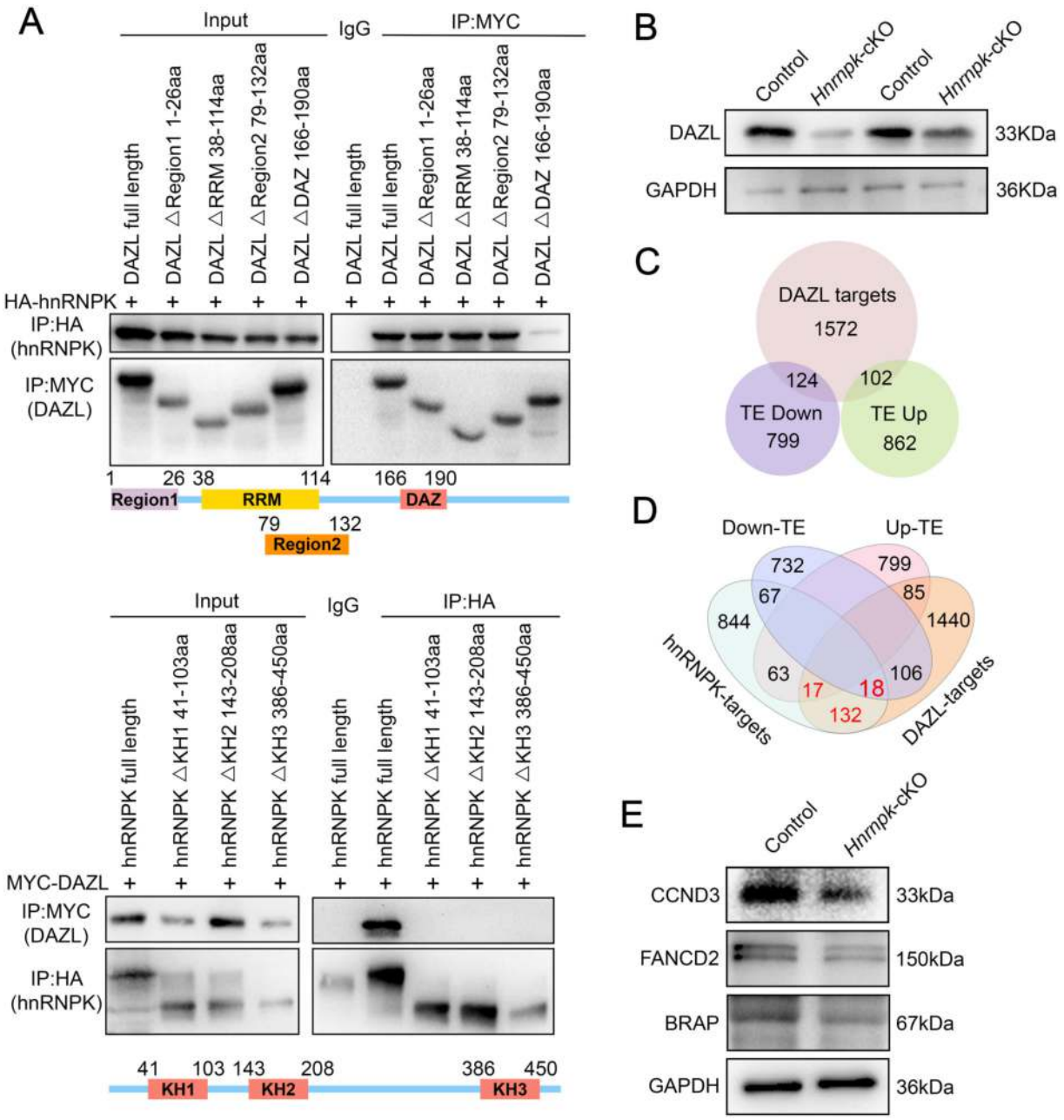

Figure 7. Translational dysregulation of DAZL target genes in hnRNPK-deficient germ cells. (**A**) Truncation mutants of DAZL (upper) and hnRNPK (lower) were expressed in HEK293T cells, and their interaction domains were validated via co-IP. The bottom schematic illustrates the domain structure of both proteins. (**B**) Western blot shows reduced DAZL protein levels in c-KIT$^+$ germ cells from Hnrnpk-cKO mice compared to controls. (**C**) Venn diagram shows the overlap between DAZL target genes and genes with altered TE in Hnrnpk-cKO c-KIT$^+$ germ cells. (**D**) Venn diagram showing the overlap among hnRNPK target genes, DAZL target genes, and genes exhibiting altered TE. (**E**) Western blot analysis in c-KIT$^+$ spermatogonia protein levels of genes co-targeted by DAZL and hnRNPK with decreased TE.

cell development. To characterize hnRNPK-dependent splicing regulation, we performed a comprehensive analysis of AS events in c-KIT$^+$ germ cells using the Multivariate Analysis of Transcript Splicing (rMATS) tool. A total of 859 differential splicing events affecting 802 genes were identified (Fig. 8A and Supplementary Table S11). Among these, SE events were the most prevalent, accounting for 629 events (68.44%), followed by alternative 3′ splice sites (A3SS, 9.14%), mutually exclusive exons (MXE, 9.03%), retained introns (RI, 8.05%), and alternative 5′ splice sites (A5SS, 5.33%) (Fig. 8A and B). Functional annotation revealed that many of the alternatively spliced genes are involved in meiotic progression, spermatogonial differentiation, and cell cycle regulation (Fig. 8C). Cross-referencing these events with our hnRNPK-RIP-seq dataset revealed that 75 differentially spliced genes are hnRNPK-bound targets (Fig. 8D). GO enrichment analysis indicated that these genes are predominantly associated with meiosis, transcriptional regulation, and spermatogenesis (Fig. 8E). Due to the prevalence of SE events among the AS categories, we concentrated our validation efforts on this splicing class. Six genes previously implicated in spermatogenesis—*Tdrd9* [59, 60], *Scml2* [61], *Stra8* [62], *Tex14* [63], *Piwil2* [64], and *Smc5*

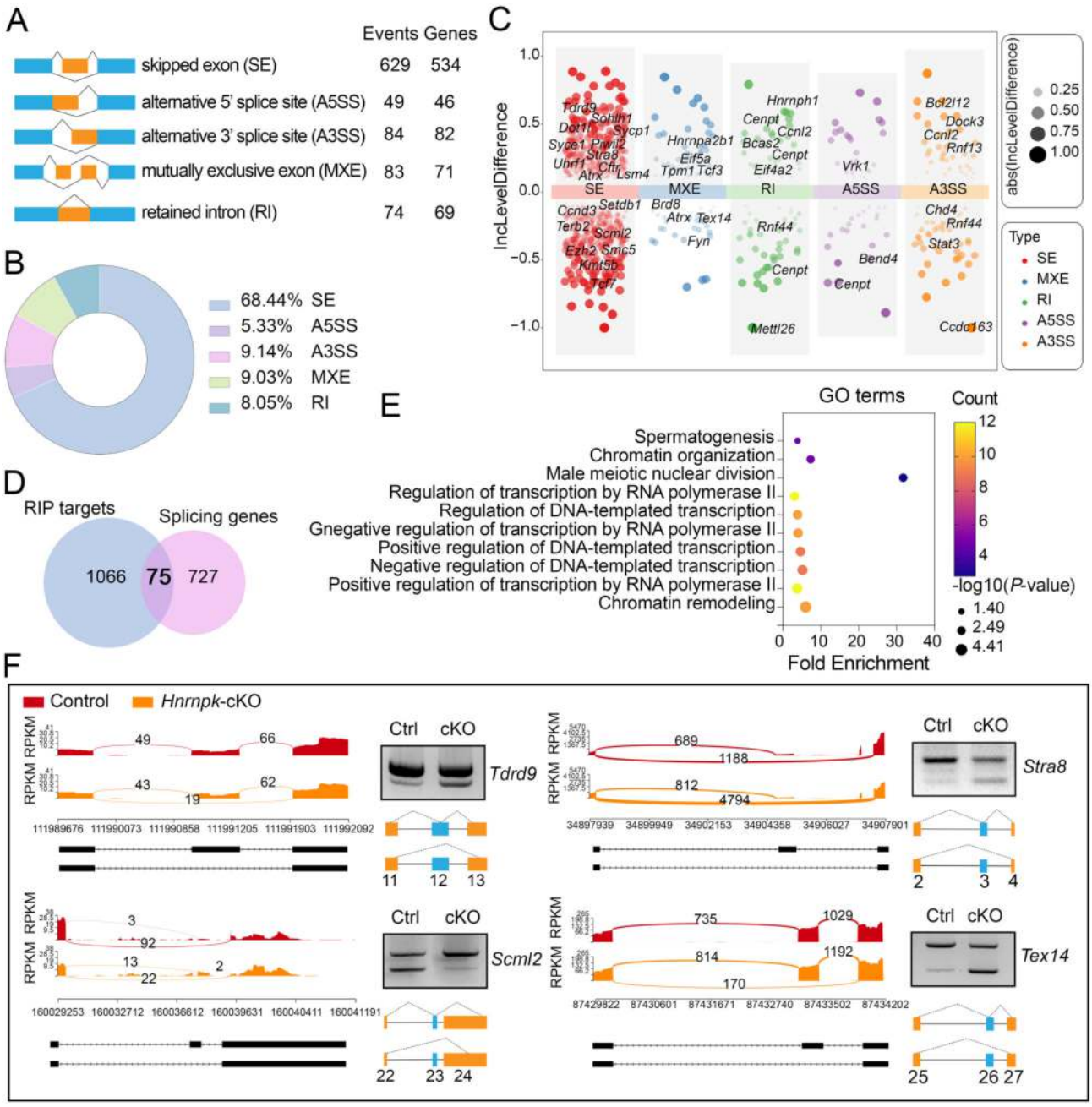

Figure 8. Aberrant mRNA splicing profiles emerge in c-KIT$^+$ germ cells upon hnRNPK deletion. (**A**) Quantification of five major types of AS events significantly affected by hnRNPK deletion in c-KIT$^+$ germ cells. The number of predicted AS events and the associated gene counts for each splicing category are listed on the right side. (**B**) Pie chart summarizes the proportion of regulated splicing events across different AS types in control and *Hnrnpk*-cKO c-KIT$^+$ germ cells. (**C**) Volcano plot illustrates differential inclusion levels of various ASEs between *Hnrnpk*-cKO c-KIT$^+$ germ cells and control group. (**D**) Venn diagram illustrates the overlap between hnRNPK-interacting transcripts and genes undergoing AS regulation. (**E**) GO enrichment analysis of overlapping genes from panel (D). (**F**) Representative Sashimi plots show differential splicing events in selected hnRNPK-bound genes from RNA-seq data of control and *Hnrnpk*-cKO c-KIT$^+$ germ cells. Validation was performed via RT-PCR in sorted c-KIT$^+$ germ cells. Exon-intron structures of target genes are illustrated below.

[65], among others—were selected for RT-PCR validation in c-KIT$^+$ germ cells. Of these, *Tdrd9*, *Scml2*, *Stra8*, and *Tex14* were also identified as direct hnRNPK interactors and exhibited clear splicing abnormalities in the *Hnrnpk*-cKO mice (Fig. 8F). Taken together, these results suggest that, in the nucleus, hnRNPK may serve as a critical regulator of the AS of transcriptional and meiosis-associated transcripts in differentiating spermatogonia, thereby ensuring the fidelity of male germline development.

Discussion

In the current study, we used a *Stra8*-GFPCre-induced germ cell-specific hnRNPK conditional knockout mouse model, alongside multi-omics analyses (scRNA-seq, RIP-seq, IP-MS, Ribo-seq, etc.), to investigate the function of hnRNPK in male germ cell development and fertility. Our findings provide significant insight into the function and regulatory mechanisms of hnRNPK, particularly with regard to its impact on the de-

velopment of differentiating spermatogonia. The loss of hnRNPK in germ cells caused male infertility in mice, accompanied by a substantial decrease in the number of differentiating spermatogonia, with only a few pre-leptotene spermatocytes observed. The results indicate that loss of hnRNPK leads to aberrant development of differentiating spermatogonia, resulting in a block in spermatogonial differentiation and meiosis entry. A previous study has also observed meiotic arrest after hnRNPK deletion [34], but the results of the present study show that the block occurs earlier in germ cell development. This difference may be due to the different timing of Cre activation in the two systems. As *Stra8* transcript is present in undifferentiated spermatogonia, the *Stra8*-GFPCre [36] transgene is likely to be activated at an earlier stage than the *Stra8*-Cre system used in the previous study [34]. Furthermore, the *Ddx4-Cre*^{ERT2} tamoxifen-inducible knockout model confirmed the crucial role of hnRNPK in meiosis entry. The present observations corroborate earlier findings and further clarify the role of hnRNPK in regulating differentiating spermatogonial development. It is also worthy of note that hnRNPK deletion in female mice results in infertility, with germ cell loss occurring as early as P1 (data not shown). This indicates an essential role for hnRNPK in female germ cell survival or maintenance. In contrast to the process in males, female meiosis occurs during the early stages of embryonic development and does not involve germline stem cells. Thus, our findings suggest that hnRNPK is implicated in regulating the meiotic processes in both male and female germ cells. However, further investigation is required to elucidate the precise mechanisms by which it exerts its regulatory function, given the distinct nature of these mechanisms.

Of note, our scRNA-seq data revealed a significant reduction in germ cell populations and identified a distinct population of apoptotic germ cells in the *Hnrnpk*-cKO mice, which was largely absent in control mice. Due to intrinsic limitations of scRNA-seq in capturing dying cells, a substantial proportion of apoptotic cells may have been lost during the preprocessing stage [66]. Nonetheless, a small cluster of cells in the *Hnrnpk*-cKO mice exhibited high expression of apoptosis-related genes, suggesting that widespread apoptosis occurs in *Hnrnpk*-cKO testes. This observation is consistent with the results of the TUNEL staining, despite the fact that the scRNA-seq data does not fully reflect the extent of apoptosis. Interestingly, our scRNA-seq analysis identified three distinct subpopulations of differentiating spermatogonia, one of which—designated DSPG3—was predominantly present in *Hnrnpk*-cKO testes. This population exhibited a strong proximity to an apoptotic germ cell cluster that had not been previously described [42, 67], primarily due to the fact that previous studies had relied on wild-type models for spermatogonial classification. By contrast, our knockout model revealed a distinct population of differentiating spermatogonia displaying transcriptional signatures indicative of apoptosis. Trajectory inference revealed that, in control mice, DSPG1 cells transition through DSPG2 before differentiating into spermatocytes. However, in the absence of hnRNPK, DSPG1 cells transition toward a DSPG3 fate characterized by apoptotic gene expression. Although the exact point in development at which DSPG3 cells appear in the testis is unclear, our data clearly support a model in which hnRNPK deficiency causes these cells to follow an abnormal, apoptotic trajectory.

Despite the prevailing hypothesis that hnRNPK is predominantly nuclear in germ cells, this study has revealed cytoplasmic localization. Intriguingly, in the cytoplasm, hnRNPK was found to interact with DAZL, a germ cell-specific translational regulator. Furthermore, a single, longer isoform of hnRNPK was identified within the cytoplasm by means of western blot analysis, thereby indicating that the cytoplasmic form of hnRNPK may be subject to specific post-translational modifications. This assertion is further substantiated by the findings of prior studies, which have indicated that phosphorylation of hnRNPK at serine residues S284 and S353 exerts a regulatory influence on its function in translational function [68, 69]. Recent studies have demonstrated that glycosylation plays a crucial role in regulating the nuclear-cytoplasmic shuttling of hnRNPK [70]. In addition, it has been established that hnRNPK is subject to methylation [71] and sumoylation [72], which may consequently affect its subcellular location and regulatory functions in gene expression. However, the precise modifications involved in germ cells remain to be elucidated.

As anticipated, the present study revealed that hnRNPK predominantly binds to the CDS and 3′ UTRs of target RNAs in c-KIT$^+$ cells [73]. However, analysis of *Hnrnpk*-cKO germ cells using RNA-seq and scRNA-seq revealed that only a small subset of transcriptionally dysregulated genes were direct targets of hnRNPK, suggesting that its primary role may lie in post-transcriptional regulation. Notably, the 3′ UTR is known to be involved in translation by recruiting translation initiation factors and ribosomal proteins [74, 75], thereby stabilizing the formation of the translation initiation complex. In this study, we also found that hnRNPK interacts with the ribosomal proteins RPS3A and RPL13, as well as the translation initiation factors eIF4A1 and eIF4A3 in c-KIT$^+$ cells. This supports the idea that hnRNPK plays a role in regulating translation during germ cell development. In addition, polysome profiling revealed that hnRNPK can be detected in the fraction containing the 40S ribosomal subunit, but is not present in the polysome fraction. Furthermore, protein synthesis assays confirmed that hnRNPK knockdown led to a reduction in *de novo* protein synthesis. The findings, when considered collectively, suggested that hnRNPK participates in the translational process by regulating the initiation phase. Ribo-seq analysis revealed that TE is disrupted in c-KIT$^+$ differentiating spermatogonia from *Hnrnpk*-cKO mice, further confirming its essential role in translational process *in vivo*. Interestingly, the TE of a large number of genes involved in transcriptional regulation, cell cycle progression, and meiosis decreased. These genes include *Brd4* [48], *Atf7* [51], *Tcf7l1* [52], and *Fancd2* [58], which are involved in the regulation of transcription and the cell cycle during spermatogenesis; others include *Ccnd3* [76], which is associated with cell cycle control; *Kit* [49], a key marker and regulator of spermatogenesis; and *Smarca4* [50] and *Brap* [56], which are critical for meiosis. Our findings provide new insights, showing that hnRNPK modulates spermatogenesis by regulating the translation of meiotic and transcription-related genes. A previous study utilizing proteomic analysis of P28 testis tissues suggested the involvement of hnRNPK in the piRNA pathway [35]. In the current study, we focused on c-KIT$^+$ spermatogonia to perform a functional analysis, which provided a clearer understanding of the role of hnRNPK in germ cells by eliminating the potential confounding effects of somatic cells. Simultaneously, an upregulation in the TE of numerous genes was also observed, which appear to be unrelated to spermatogenesis. In order to explain this phenomenon, we hypothesize that, in the absence of hnRNPK, components of unused trans-

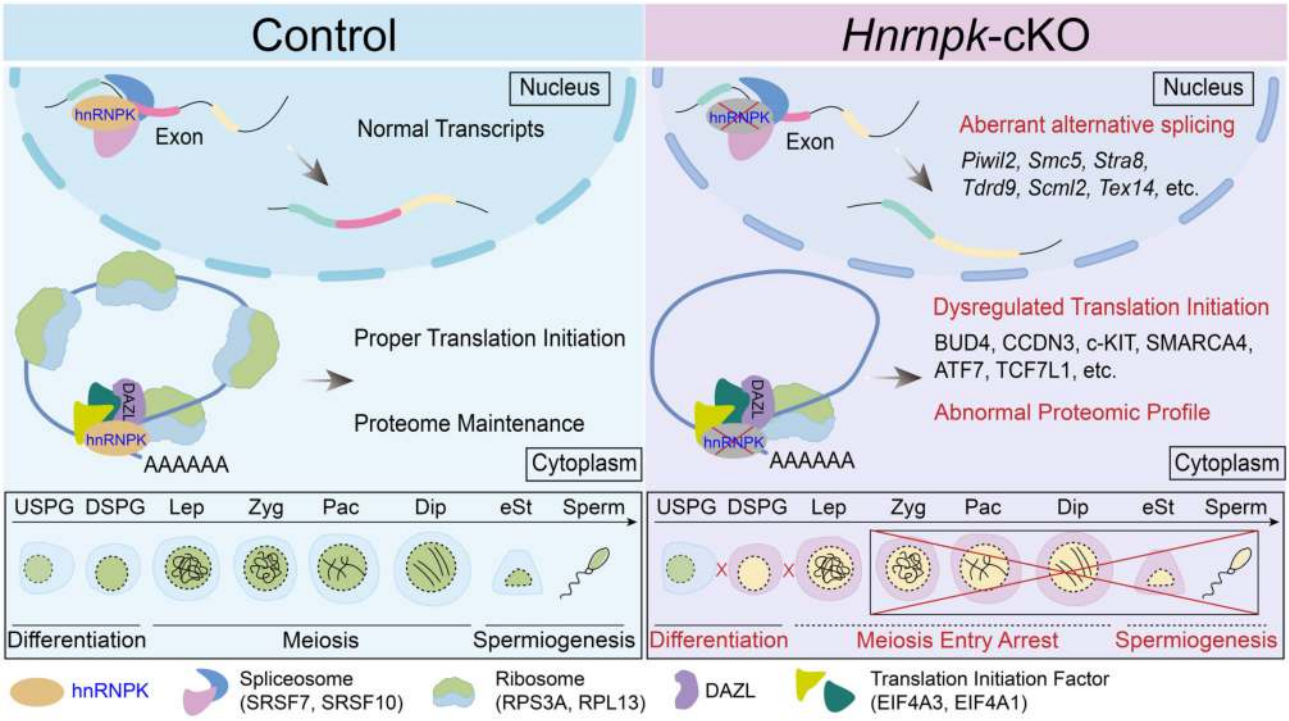

Figure 9. Mechanistic illustration of hnRNPK function in male germ cells. hnRNPK interacts with DAZL, eIF4A1, eIF4A3, RPL13, and RPS3A in the cytoplasm to orchestrate translational initiation in differentiating spermatogonia. In the nucleus, hnRNPK interacts with the splicing factors SRSF7 and SRSF10 and maintains normal spermatogenesis by regulating AS of spermatogenesis-related transcripts. Deletion of hnRNPK disrupts the translation and splicing of genes involved in meiosis, cell cycle regulation, and mRNA transcription. This results in proteomic and transcriptomic imbalances, leads to aberrant differentiating spermatogonial development, and ultimately causes male infertility.

lational machinery may be reallocated to facilitate the translation of other, non-spermatogenesis-related mRNAs. hnRNPK may contribute to the regulation of spermatogenic translation by interacting with translation initiation factors eIF4A1 and eIF4A3, and ribosomal proteins RPS3A and RPL13. However, the precise molecular mechanisms by which hnRNPK cooperates with the ribosome and these initiation factors remain to be elucidated.

Furthermore, the present study has demonstrated that hnRNPK and DAZL can be detected in the fraction containing the 40S ribosomal subunit. In addition, DAZL protein expression was reduced in the *Hnrnpk*-cKO mice, and altered TE of DAZL target RNAs was observed. These findings suggest that the loss of hnRNPK may lead to a downregulation of DAZL, subsequently resulting in dysregulation of the translation of its target mRNAs. It has been previously reported that DAZL primarily regulates TE through modulation of translational elongation [54, 55]. However, given its strong interaction with hnRNPK and shared localization at the 40S ribosomal subunit, it remains unknown whether DAZL also plays a role in regulating translation initiation.

Interestingly, we also found that genes with reduced TE in *Hnrnpk*-cKO germ cells were significantly enriched in spliceosome complex components. Moreover, our proteomic data revealed that hnRNPK interacts with splicing factors such as SRSF9 [77, 78] and SRSF10 [79], suggesting that aberrant splicing events may occur in its absence. Splicing analysis revealed numerous dysregulated AS events involving genes related to meiosis and cell cycle regulation. These include *Ccnd3* and *Ccnl2*, which are critical for cell cycle progression; *Tdrd9*, which interacts with MIWI2 and participates in meiosis [60], with mutations associated with non-obstructive azoospermia [59]; as well as *Scml2* [61], *Smc5* [65], *Stra8* [62], *Tex14* [63], and *Piwil2* [64, 80], all of which are implicated in meiotic processes. Of note, many of the direct splicing targets of hnRNPK were associated with RNA polymerase-related genes, suggesting that hnRNPK may indirectly modulate transcriptional regulation in the nucleus of germ cells by influencing the splicing of RNA polymerase-associated proteins. Whether other splicing regulators are involved in mediating the splicing of these target genes, and the specific mechanisms by which hnRNPK contributes to splicing control, remain important questions for further investigation.

In conclusion, the present study has identified hnRNPK as a critical regulator in male germ development and has revealed the underlying mechanisms in this process. The deletion of hnRNPK resulted in infertility in mice, accompanied by a significant reduction in differentiating spermatogonia and a failure to enter meiosis. scRNA-seq analysis of *Hnrnpk*-cKO testes further revealed marked alterations in the state of differentiating spermatogonia in *Hnrnpk*-cKO testes, which failed entry into meiosis. Importantly, this study reveals an important cytoplasmic function of hnRNPK in germ cells, where it colocalizes with DAZL at the 40S ribosome to regulate the initiation of target mRNA translation. Concomitantly, nuclear hnRNPK interacts with splicing factors to modulate ASEs of spermatogenesis-related transcripts. hnRNPK deficiency in c-KIT^{+} cells disrupts the initiation of translation and splicing of essential regulators of meiosis, the cell cycle, and transcriptional control. This translational impairment leads to secondary disturbances in the transcriptome and proteome, causing cell cycle arrest, blocked meiotic entry, and male infertility (Fig. 9). Our study sheds light on the functional role and mechanistic involvement of hnRNPK in male germ cell develop-

ment, providing valuable insights into the post-transcriptional regulatory mechanisms that govern these processes.

Acknowledgements

The authors thank Dr Minghan Tong (Shanghai Institute of Biochemistry and Cell Biology, Chinese Academy of Sciences) for generously sharing the *Stra8*-GFPCre transgenic mouse strain, which was essential for this study. The authors also acknowledge BioRender, the graphical abstract in this study created in BioRender (https://BioRender.com/mco30t9).

Author contributions: Huihui Gao (Conceptualization [equal], Investigation [equal], Methodology [equal], Validation [equal], Writing—original draft [equal]), Shiyu Yang (Conceptualization [equal], Investigation [equal], Methodology [equal], Validation [equal]), Ao Ning (Conceptualization [equal], Data curation [equal], Methodology [equal]), Lisha Yin (Investigation [equal]), Yifei Lan (Investigation [equal]), Keren Cheng (Methodology [supporting]), Wenjing Xiong (Investigation [equal]), Xinxin Xiong (Investigation [equal]), Jin Zhang(Investigation [supporting]), Jingshou Chen (Investigation [equal]), Shenglei Feng (Investigation [equal]), Xu Fan (Investigation [equal]), Kuan Liu (Investigation [equal]), Yiqian Gui (Investigation [equal]), Peng Zhang (Investigation [equal]), Xiaoli Wang (Project administration [equal]), Fengli Wang (Project administration [equal]), Xiaoxu Chen (Investigation [equal], Methodology [equal], Supervision [equal]), Qinghua Zhang (Supervision [equal], Validation [equal]), and Shuiqiao Yuan (Supervision, Conceptialization, Investigation [equal]; Writing-revised).

Supplementary data

Supplementary data is available at NAR online.

Conflict of interest

None declared.

Funding

This work received support from the National Key Research and Development Program of China (2024YFA1108100 to S.Y.), the National Natural Science Foundation of China (82371625 to S.Y., 82302099 to X.C.), the China Postdoctoral Science Foundation (2023M742727 to H.G.), Shenzhen Natural Science Foundation in Basic Research Fund (JCYJ20240813153314019 to S.Y.), Guangdong Basic and Applied Basic Research Foundation (2024A1515012936 to S.Y.), the Hubei Provincial Laboratory Animal Research Special Fund (2023CFA006 to S.Y.), the Funding for Scientific Research Projects from Wuhan Municipal Health Commission (WX23A47 to P.Z.), and the Basic Research Support Program of Huazhong University of Science and Technology (2023BR031 to S.Y.). Funding to pay the Open Access publication charges for this article was provided by the National Key Research and Development Program of China (2024YFA1108100).

Data availability

The single-cell sequencing data are available in the NCBI database under accession number PRJNA1283936 (related to Fig. 3 and Supplementary Figs S6--S9). The RNA-seq and RIP-seq data are available in the NCBI database under accession numbers PRJNA1283937 and PRJNA1283938, respectively (related to Fig. 4 and Supplementary Fig. S10). The Ribo-seq data are available in the NCBI database under accession number PRJNA1283939 (related to Fig. 5 and Supplementary Fig. S11). The MS-DIA data are available in the iProX database under the project ID IPX0012502000 (related to Fig. 6). All datasets and supporting data of this study are available from the corresponding author upon reasonable request. The graphical abstract in this study was created using BioRender (https://BioRender.com/mco30t9).

References

1. Western PS, Miles DC, van den Bergen JA *et al.* Dynamic regulation of mitotic arrest in fetal male germ cells. *Stem Cells* 2008;26:339–47. https://doi.org/10.1634/stemcells.2007-0622
2. Drumond AL, Meistrich ML, Chiarini-Garcia H. Spermatogonial morphology and kinetics during testis development in mice: a high-resolution light microscopy approach. *Reproduction* 2011;142:145–55. https://doi.org/10.1530/REP-10-0431
3. Busada JT, Kaye EP, Renegar RH *et al.* Retinoic acid induces multiple hallmarks of the prospermatogonia-to-spermatogonia transition in the neonatal mouse. *Biol Reprod* 2014;90:64. https://doi.org/10.1095/biolreprod.113.114645
4. Niedenberger BA, Busada JT, Geyer CB. Marker expression reveals heterogeneity of spermatogonia in the neonatal mouse testis. *Reproduction* 2015;149:329–38. https://doi.org/10.1530/REP-14-0653
5. Snyder EM, Small C, Griswold MD. Retinoic acid availability drives the asynchronous initiation of spermatogonial differentiation in the mouse. *Biol Reprod* 2010;83:783–90. https://doi.org/10.1095/biolreprod.110.085811
6. Zhou Q, Nie R, Li Y *et al.* Expression of stimulated by retinoic acid gene 8 (Stra8) in spermatogenic cells induced by retinoic acid: an *in vivo* study in vitamin A-sufficient postnatal murine testes. *Biol Reprod* 2008;79:35–42. https://doi.org/10.1095/biolreprod.107.066795
7. Schrans-Stassen BH, van de Kant HJ, de Rooij DG *et al.* Differential expression of c-kit in mouse undifferentiated and differentiating type A spermatogonia. *Endocrinology* 1999;140:5894–900. https://doi.org/10.1210/endo.140.12.7172
8. O'Donnell L. Mechanisms of spermiogenesis and spermiation and how they are disturbed. *Spermatogenesis* 2014;4:e979623. https://doi.org/10.4161/21565562.2014.979623
9. Mithraprabhu S, Loveland KL. Control of KIT signalling in male germ cells: what can we learn from other systems? *Reproduction* 2009;138:743–57. https://doi.org/10.1530/REP-08-0537
10. O'Bryan MK, de Kretser D. Mouse models for genes involved in impaired spermatogenesis. *Int J of Andrology* 2006;29:76–89. https://doi.org/10.1111/j.1365-2605.2005.00614.x
11. Nieschlag E, Nieschlag E, Behre HM *et al. Andrology: Male Reproductive Health and Dysfunction*. Cham: Springer International Publishing: Imprint: Springer, 2023. https://doi.org/10.1007/978-3-031-31574-9
12. Dreyfuss G, Matunis MJ, Pinol-Roma S *et al.* hnRNP proteins and the biogenesis of mRNA. *Annu Rev Biochem* 1993;62:289–321. https://doi.org/10.1146/annurev.bi.62.070193.001445
13. Han SP, Tang YH, Smith R. Functional diversity of the hnRNPs: past, present and perspectives. *Biochem J* 2010;430:379–92. https://doi.org/10.1042/BJ20100396
14. Wang XL, Li JM, Yuan SQ. Characterization of the protein expression and localization of hnRNP family members during murine spermatogenesis. *Asian J Androl* 2023;25:314–21. https://doi.org/10.4103/aja202273
15. Ehrmann I, Dalgliesh C, Tsaousi A *et al.* Haploinsufficiency of the germ cell-specific nuclear RNA binding protein hnRNP G-T

prevents functional spermatogenesis in the mouse. *Hum Mol Genet* 2008;17:2803–18. https://doi.org/10.1093/hmg/ddn179
16. Li J, Guo W, Li F *et al.* HnRNPL as a key factor in spermatogenesis: lesson from functional proteomic studies of azoospermia patients with sertoli cell only syndrome. *J Proteomics* 2012;75:2879–91. https://doi.org/10.1016/j.jprot.2011.12.040
17. Feng S, Li J, Wen H *et al.* hnRNPH1 recruits PTBP2 and SRSF3 to modulate alternative splicing in germ cells. *Nat Commun* 2022;13:3588. https://doi.org/10.1038/s41467-022-31364-7
18. Wen Y, Zhou S, Gui Y *et al.* hnRNPU is required for spermatogonial stem cell pool establishment in mice. *Cell Rep* 2024;43:114113. https://doi.org/10.1016/j.celrep.2024.114113
19. Wang X, Fan X, Zhang J *et al.* hnRNPA2B1 represses the disassembly of arsenite-induced stress granules and is essential for male fertility. *Cell Rep* 2024;43:113769. https://doi.org/10.1016/j.celrep.2024.113769
20. Lv P, Xu W, Xin S *et al.* HnRNPM modulates alternative splicing in germ cells by recruiting PTBP1. *Reprod Biol Endocrinol* 2025;23:3. https://doi.org/10.1186/s12958-024-01340-5
21. Xiong X, Feng S, Ma X *et al.* hnRNPC functions with HuR to regulate alternative splicing in an m^{6}A-dependent manner and is essential for meiosis. *Adv Sci* 2025;12:e2412196. https://doi.org/10.1002/advs.202412196
22. Feng S, Wen H, Liu K *et al.* hnRNPH1 establishes Sertoli–germ cell crosstalk through cooperation with PTBP1 and AR, and is essential for male fertility in mice. *Development* 2023;150:dev201040. https://doi.org/10.1242/dev.201040
23. Valverde R, Edwards L, Regan L. Structure and function of KH domains. *FEBS J* 2008;275:2712–26. https://doi.org/10.1111/j.1742-4658.2008.06411.x
24. Wang Z, Qiu H, He J *et al.* The emerging roles of hnRNPK. *J Cell Physioyl* 2020;235:1995–2008. https://doi.org/10.1002/jcp.29186
25. Gallardo M, Lee HJ, Zhang X *et al.* hnRNP K is a haploinsufficient tumor suppressor that regulates proliferation and differentiation programs in hematologic malignancies. *Cancer Cell* 2015;28:486–99. https://doi.org/10.1016/j.ccell.2015.09.001
26. Michelotti EF, Michelotti GA, Aronsohn AI *et al.* Heterogeneous nuclear ribonucleoprotein K is a transcription factor. *Mol Cell Biol* 1996;16:2350–60. https://doi.org/10.1128/MCB.16.5.2350
27. Takimoto M, Tomonaga T, Matunis M *et al.* Specific binding of heterogeneous ribonucleoprotein particle protein K to the human c-myc promoter, *in vitro*. *J Biol Chem* 1993;268:18249–58. https://doi.org/10.1016/S0021-9258(17)46837-2
28. Ritchie SA, Pasha MK, Batten DJ *et al.* Identification of the SRC pyrimidine-binding protein (SPy) as hnRNP K: implications in the regulation of SRC1A transcription. *Nucleic Acids Res* 2003;31:1502–13. https://doi.org/10.1093/nar/gkg246
29. Evans JR, Mitchell SA, Spriggs KA *et al.* Members of the poly (rC) binding protein family stimulate the activity of the c-myc internal ribosome entry segment *in vitro* and *in vivo*. *Oncogene* 2003;22:8012–20. https://doi.org/10.1038/sj.onc.1206645
30. Xu Y, Wu W, Han Q *et al.* Post-translational modification control of RNA-binding protein hnRNPK function. *Open Biol* 2019;9:180239. https://doi.org/10.1098/rsob.180239
31. Peng WZ, Liu JX, Li CF *et al.* hnRNPK promotes gastric tumorigenesis through regulating CD44E alternative splicing. *Cancer Cell Int* 2019;19:335. https://doi.org/10.1186/s12935-019-1020-x
32. Yamamoto K, Furukawa MT, Fukumura K *et al.* Control of the heat stress-induced alternative splicing of a subset of genes by hnRNP K. *Genes Cells* 2016;21:1006–14. https://doi.org/10.1111/gtc.12400
33. Liu S, Duan Y, You R *et al.* HnRNP K regulates inflammatory gene expression by mediating splicing pattern of transcriptional factors. *Exp Biol Med (Maywood)* 2023;248:1479–91. https://doi.org/10.1177/15353702221110649
34. Xu H, Guo J, Wu W *et al.* Deletion of *Hnrnpk* gene causes infertility in male mice by disrupting spermatogenesis. *Cells* 2022;11:1277.
35. Xu H, Guo J, Huang Y *et al.* Insights into the role of hnRNPK in spermatogenesis via the piRNA pathway. *Sci Rep* 2025;15:6438. https://doi.org/10.1038/s41598-025-91081-1
36. Lin Z, Hsu PJ, Xing X *et al.* Mettl3-/Mettl14-mediated mRNA N^6-methyladenosine modulates murine spermatogenesis. *Cell Res* 2017;27:1216–30. https://doi.org/10.1038/cr.2017.117
37. Li P, Tang J, Yu Z *et al.* CHD4 acts as a critical regulator in the survival of spermatogonial stem cells in micedagger. *Biol Reprod* 2022;107:1331–44.
38. Goodyear S, Brinster R. Isolation of the spermatogonial stem cell-containing fraction from testes. *Cold Spring Harb Protoc* 2017;2017:pdb.prot094185. https://doi.org/10.1101/pdb.prot094185
39. Zhou Y, Zhou B, Pache L *et al.* Metascape provides a biologist-oriented resource for the analysis of systems-level datasets. *Nat Commun* 2019;10:1523. https://doi.org/10.1038/s41467-019-09234-6
40. Shen S, Park JW, Lu ZX *et al.* rMATS: robust and flexible detection of differential alternative splicing from replicate RNA-seq data. *Proc Natl Acad Sci USA* 2014;111:E5593–601. https://doi.org/10.1073/pnas.1419161111
41. Shen S, Park JW, Huang J *et al.* MATS: a Bayesian framework for flexible detection of differential alternative splicing from RNA-seq data. *Nucleic Acids Res* 2012;40:e61. https://doi.org/10.1093/nar/gkr1291
42. Chen Y, Zheng Y, Gao Y *et al.* Single-cell RNA-seq uncovers dynamic processes and critical regulators in mouse spermatogenesis. *Cell Res* 2018;28:879–96. https://doi.org/10.1038/s41422-018-0074-y
43. Ishiguro KI. Mechanisms of meiosis initiation and meiotic prophase progression during spermatogenesis. *Mol Aspects Med* 2024;97:101282. https://doi.org/10.1016/j.mam.2024.101282
44. Leskov KS, Klokov DY, Li J *et al.* Synthesis and functional analyses of nuclear clusterin, a cell death protein. *J Biol Chem* 2003;278:11590–600. https://doi.org/10.1074/jbc.M209233200
45. Shannan B, Seifert M, Boothman DA *et al.* Clusterin and DNA repair: a new function in cancer for a key player in apoptosis and cell cycle control. *J Mol Hist* 2006;37:183–8. https://doi.org/10.1007/s10735-006-9052-7
46. Yin X, Zhang P, Xia N *et al.* GPx8 regulates apoptosis and autophagy in esophageal squamous cell carcinoma through the IRE1/JNK pathway. *Cell Signalling* 2022;93:110307. https://doi.org/10.1016/j.cellsig.2022.110307
47. Bossy-Wetzel E, Bakiri L, Yaniv M. Induction of apoptosis by the transcription factor c-Jun. *EMBO J* 1997;16:1695–709. https://doi.org/10.1093/emboj/16.7.1695
48. Dey A, Ellenberg J, Farina A *et al.* A bromodomain protein, MCAP, associates with mitotic chromosomes and affects G(2)-to-M transition. *Mol Cell Biol* 2000;20:6537–49. https://doi.org/10.1128/.20.17.6537-6549.2000
49. Rossi P, Sette C, Dolci S *et al.* Role of c-kit in mammalian spermatogenesis. *J Endocrinol Invest* 2000;23:609–15. https://doi.org/10.1007/BF03343784
50. Kim Y, Fedoriw AM, Magnuson T. An essential role for a mammalian SWI/SNF chromatin-remodeling complex during male meiosis. *Development* 2012;139:1133–40. https://doi.org/10.1242/dev.073478
51. Liu Y, Maekawa T, Yoshida K *et al.* The transcription factor ATF7 mediates in vitro fertilization-induced gene expression changes in mouse liver. *FEBS Open Bio* 2017;7:1598–610. https://doi.org/10.1002/2211-5463.12304
52. Bu L, Yang Q, McMahon L *et al.* Wnt suppressor and stem cell regulator TCF7L1 is a sensitive immunohistochemical marker to differentiate testicular seminoma from non-seminomatous germ cell tumor. *Exp Mol Pathol* 2019;110:104293. https://doi.org/10.1016/j.yexmp.2019.104293
53. Zagore LL, Sweet TJ, Hannigan MM *et al.* DAZL regulates germ cell survival through a network of PolyA-proximal mRNA

interactions. *Cell Rep* 2018;25:1225–40. https://doi.org/10.1016/j.celrep.2018.10.012
54. Mikedis MM, Fan Y, Nicholls PK *et al.* DAZL mediates a broad translational program regulating expansion and differentiation of spermatogonial progenitors. *eLife* 2020;9:e56523. https://doi.org/10.7554/eLife.56523
55. Li H, Liang Z, Yang J *et al.* DAZL is a master translational regulator of murine spermatogenesis. *Natl Sci Rev* 2019;6:455–68. https://doi.org/10.1093/nsr/nwy163
56. D'Amora DR, Hu Q, Pizzardi M *et al.* BRAP-2 promotes DNA damage induced germline apoptosis in C. elegans through the regulation of SKN-1 and AKT-1. *Cell Death Differ* 2018;25:1276–88. https://doi.org/10.1038/s41418-017-0038-7
57. Feng LX, Ravindranath N, Dym M. Stem cell factor/c-kit up-regulates cyclin D3 and promotes cell cycle progression via the phosphoinositide 3-kinase/p70 S6 kinase pathway in spermatogonia. *J Biol Chem* 2000;275:25572–6. https://doi.org/10.1074/jbc.M002218200
58. Zhao S, Huang C, Yang Y *et al.* DNA repair protein FANCD2 has both ubiquitination-dependent and ubiquitination-independent functions during germ cell development. *J Biol Chem* 2023;299:102905. https://doi.org/10.1016/j.jbc.2023.102905
59. Arafat M, Har-Vardi I, Harlev A *et al.* Mutation in TDRD9 causes non-obstructive azoospermia in infertile men. *J Med Genet* 2017;54:633–9. https://doi.org/10.1136/jmedgenet-2017-104514
60. Shoji M, Tanaka T, Hosokawa M *et al.* The TDRD9–MIWI2 complex is essential for piRNA-mediated retrotransposon silencing in the mouse male germline. *Dev Cell* 2009;17:775–87. https://doi.org/10.1016/j.devcel.2009.10.012
61. Luo M, Zhou J, Leu NA *et al.* Polycomb protein SCML2 associates with USP7 and counteracts histone H2A ubiquitination in the XY chromatin during male meiosis. *PLoS Genet* 2015;11:e1004954. https://doi.org/10.1371/journal.pgen.1004954
62. Mark M, Jacobs H, Oulad-Abdelghani M *et al.* STRA8-deficient spermatocytes initiate, but fail to complete, meiosis and undergo premature chromosome condensation. *J Cell Sci* 2008;121:3233–42. https://doi.org/10.1242/jcs.035071
63. Greenbaum MP, Yan W, Wu MH *et al.* TEX14 is essential for intercellular bridges and fertility in male mice. *Proc Natl Acad Sci USA* 2006;103:4982–7. https://doi.org/10.1073/pnas.0505123103
64. Aravin AA, Sachidanandam R, Girard A *et al.* Developmentally regulated piRNA clusters implicate MILI in transposon control. *Science* 2007;316:744–7. https://doi.org/10.1126/science.1142612
65. Hwang G, Verver DE, Handel MA *et al.* Depletion of SMC5/6 sensitizes male germ cells to DNA damage. *MBoC* 2018;29:3003–16. https://doi.org/10.1091/mbc.E18-07-0459
66. Ordonez-Rueda D, Baying B, Pavlinic D *et al.* Apoptotic cell exclusion and bias-free single-cell selection are important quality control requirements for successful single-cell sequencing applications. *Cytometry Pt A* 2020;97:156–67. https://doi.org/10.1002/cyto.a.23898
67. Ernst C, Eling N, Martinez-Jimenez CP *et al.* Staged developmental mapping and X chromosome transcriptional dynamics during mouse spermatogenesis. *Nat Commun* 2019;10:1251. https://doi.org/10.1038/s41467-019-09182-1
68. Huang WS, Xu FM, Zeng QZ *et al.* ERK1/2-mediated cytoplasmic accumulation of hnRNPK antagonizes TRAIL-induced apoptosis through upregulation of XIAP in H1299 cells. *Biomed Environ Sci* 2017;30:473–81.
69. Habelhah H, Shah K, Huang L *et al.* ERK phosphorylation drives cytoplasmic accumulation of hnRNP-K and inhibition of mRNA translation. *Nat Cell Biol* 2001;3:325–30. https://doi.org/10.1038/35060131
70. Phoomak C, Park D, Silsirivanit A *et al.* O-GlcNAc-induced nuclear translocation of hnRNP-K is associated with progression and metastasis of cholangiocarcinoma. *Mol Oncol* 2019;13:338–57. https://doi.org/10.1002/1878-0261.12406
71. Chang YI, Hsu SC, Chau GY *et al.* Identification of the methylation preference region in heterogeneous nuclear ribonucleoprotein K by protein arginine methyltransferase 1 and its implication in regulating nuclear/cytoplasmic distribution. *Biochem Biophys Res Commun* 2011;404:865–9. https://doi.org/10.1016/j.bbrc.2010.12.076
72. Li T, Evdokimov E, Shen RF *et al.* Sumoylation of heterogeneous nuclear ribonucleoproteins, zinc finger proteins, and nuclear pore complex proteins: a proteomic analysis. *Proc Natl Acad Sci USA* 2004;101:8551–6. https://doi.org/10.1073/pnas.0402889101
73. Geuens T, Bouhy D, Timmerman V. The hnRNP family: insights into their role in health and disease. *Hum Genet* 2016;135:851–67. https://doi.org/10.1007/s00439-016-1683-5
74. Kuersten S, Goodwin EB. The power of the 3′ UTR: translational control and development. *Nat Rev Genet* 2003;4:626–37. https://doi.org/10.1038/nrg1125
75. de Moor CH, Meijer H, Lissenden S. Mechanisms of translational control by the 3' UTR in development and differentiation. *Semin Cell Dev Biol* 2005;16:49–58. https://doi.org/10.1016/j.semcdb.2004.11.007
76. Chotiner JY, Wolgemuth DJ, Wang PJ. Functions of cyclins and CDKs in mammalian gametogenesisdagger. *Biol Reprod* 2019;101:591–601. https://doi.org/10.1093/biolre/ioz070
77. Ha J, Jang H, Choi N *et al.* SRSF9 regulates cassette exon splicing of caspase-2 by interacting with its downstream exon. *Cells* 2021;10:679. https://doi.org/10.3390/cells10030679 .
78. Jiang N, Li Y, Yin L *et al.* The intricate functional networks of pre-mRNA alternative splicing in mammalian spermatogenesis. *Int J Mol Sci* 2024;25:12074. https://doi.org/10.3390/ijms252212074 .
79. Liu W, Lu X, Zhao ZH *et al.* SRSF10 is essential for progenitor spermatogonia expansion by regulating alternative splicing. *eLife* 2022;11:e78211. https://doi.org/10.7554/eLife.78211
80. Di Giacomo M, Comazzetto S, Saini H *et al.* Multiple epigenetic mechanisms and the piRNA pathway enforce LINE1 silencing during adult spermatogenesis. *Mol Cell* 2013;50:601–8. https://doi.org/10.1016/j.molcel.2013.04.026

Received: July 24, 2025. **Revised:** January 21, 2026. **Accepted:** January 25, 2026